

# Ground-based observations of the cyclic nature in planetary-scale cloud features associated with Venus super-rotation

Masataka Imai

Student ID number: 20133073

Planetary and Space Group, Department of CosmoSciences,  
Graduate School of Science, Hokkaido University

Supervisor : Yukihiro Takahashi

2015/02/27

## Abstract

The dynamical mechanism of Venusian super-rotation remains a mystery for a long time. This phenomenon is that the Venus atmosphere around 60 km cloud level moves westward at a velocity 60 times faster than the planetary rotation. Previous studies suggest planetary scale waves are associated with the super-rotation [e.g. Yamamoto and Tanaka, 1997]. Also these waves are considered to form planetary scale UV features (named “Y-feature”) in the cloud top. Pioneer Venus spacecraft observed the periodical variation of UV brightness with the period 4-5 days which caused by that the propagation of planetary scale UV features [Del Genio and Rossow, 1982, 1990]. They suggested that the period of brightness variation corresponds to the propagation of planetary waves and it changes on a time scale of 5-10 years. Periodicity change can be argued as the vacillation of dynamical states and investigating the source of planetary waves is required to understand the super-rotation.

We conducted ground-based Venus observations at one month intervals from mid-August 2013 to the end of June 2014. Pioneer Venus’s useful images exist for no longer than about three months out of every Venus year (225 Earth days). On the other hand, our observations cover about one Venus year and have a superiority for investigating the monthly change. Used instrument is an imager with 365 nm narrow-band filter installed on 1.6m Pirka telescope, which constructed and operated by Hokkaido University, and we measured the UV brightness from equatorial to mid-latitudinal regions in both hemispheres. We confirmed that the result of UV brightness variation from our ground-based observations have good correlations with those from the Venus Monitoring Camera (VMC) on-board Venus Express spacecraft. The VMC captured UV features in global scale only in the southern hemisphere because Venus Express is in elliptic orbit with apocenter in the southern hemisphere.

From our results, we revealed that the periodicity in the UV brightness variation changes within a Venus year. In our observational period, we have two seasons when the brightness has the periodical variation. Latter season is considered to keep the periodicity for about two months. In August 2013, we detected about 5.2 days periodical brightness changes in equatorial and both northern and southern mid-latitudinal region. Bright and dark pattern had a prominent periodical and symmetric structure about the equator and we consider it is derived from a high contrast Y-feature such as previously observed by the Galileo spacecraft. On the other hand, after the mid-September 2013, there was no prominent and periodical brightness variation in the most of the observation time. In this season, the periodical and

symmetric brightness structure has a cycle of being clear and unclear, and it suggests the Y-feature is not always dominant. We also detected that boundaries of bright and dark region exist near the latitudes of  $30^\circ$  N and  $30^\circ$  S when the periodical and symmetric brightness structure can be seen. It can be regarded as one of the manifestation of the existence of planetary waves. The absence of the periodical variation seems to continue by the end of March 2014. In the last two months (from the beginning of May to the end of June 2014), however, it has 3.5 days period and perhaps last for about two months. Our study points out the possibility of the change of dynamical states occurs in one Venus year.

---

## Contents

<b>1</b>	<b>Introduction</b>	<b>2</b>
1.1	Superrotation . . . . .	3
1.2	Y-feature . . . . .	7
1.3	Atmospheric waves in Venus . . . . .	10
1.4	Purpose of this study . . . . .	17
<b>2</b>	<b>Observation and Data</b>	<b>21</b>
2.1	Pirka telescope and Multi-Spectral Imager(MSI) . . . . .	23
2.2	Observation from satellites . . . . .	28
<b>3</b>	<b>Analysis for ground-based images</b>	<b>29</b>
3.1	Bias and Flat reduction . . . . .	29
3.2	Determination of the Venus geographical coordinates . . . . .	30
3.3	Determination discrepancies of Venus geographical coordinates	40
3.4	Evaluate the seeing effect . . . . .	43
3.5	Methods to subtract extinction effect of the Earth's atmosphere and measure the brightness variation . . . . .	46
3.6	Test analysis for the Galileo images . . . . .	49
<b>4</b>	<b>Results</b>	<b>51</b>
4.1	Comparison of the brightness variation between MSI and VMC	51
4.2	Fluctuation of UV features . . . . .	54
4.3	Periodicity of the UV brightness variation . . . . .	57
<b>5</b>	<b>Discussion</b>	<b>61</b>
<b>6</b>	<b>Summary</b>	<b>64</b>
	<b>Appendix</b>	<b>66</b>
A:	Measurement error of brightness variation . . . . .	66
B:	List of analyzed Galileo/SSI images . . . . .	69
C:	List of analyzed Venus Express/VMC images . . . . .	70
D:	Lomb-Scargle periodgram analysis . . . . .	71

# 1 Introduction

Planetary atmospheres have a great important role to determine the environment such as the temperature, humidity, pressure and so on. Venus is sometimes called "Earth's twin" because its size and the mass is similar to the Earth. However, there is no ocean in Venus and the main component of the atmosphere is carbon dioxide, which cause runaway greenhouse effect. Mean surface temperature is about 730 K (460 °C) and surface pressure is higher than 90 atmospheric pressure. Venus's quite thick atmosphere is known to move very fast against the planet's rotation and this characteristic atmospheric flow is named "Superrotation". Detail of this phenomena is described in Section 1.2 but it can be said that there are great different points of the dynamical system between in the Earth's and Venus's atmosphere therefore, from Venus, we can develop a new point of view to learn the meteorology in planets.

	Venus	Earth
Equatorial radius [km]	6052	6378
Mass [ $10^{24}$ kg]	4.87	5.97
Mean density [g/m <sup>3</sup> ]	5.24	5.52
Surface gravity [m/s <sup>2</sup> ]	8.9	9.8
Distance from the sun [AU]	0.723	1.00
Eccentricity	0.00677	0.01671
Inclination	3.39°	0°
Obliquity	177.4°	23.44°
Sidereal rotation period (Earth day)	243.0	1.00
Orbital period (Earth day)	224.7	365.2
Surface pressure [hPa]	92000	1013
Surface temperature [K]	730	288

Table 1.1: Physical parameters of Venus and the Earth

## 1.1 Superrotation

The superrotation is a phenomenon that Venusian atmosphere moves westward at a velocity 60 times faster than the planetary rotation. The atmosphere accelerates at a velocity about 100 m/s and it forms 4-day retrograde circulation. Figure 1.1 shows the westward wind velocity at various latitudes, which was directly measured by several probes descending into Venus's atmosphere. Each probe observed different local time, latitude and season. These results indicate that the zonal wind velocity increases with the increasing altitude from surface and the atmosphere is accelerated faster than 100 m/s above the cloud top (about 60–70 km). Figure 1.2 represents zonal wind velocity measured from cloud tracking with Galileo images. Measurements were conducted using the violet (418 nm) and NIR (986 nm) images appearing as black circles and crosses respectively. Violet images were analyzed with assumption that the altitude of the cloud cover is 60 km. Vertical separation between violet and NIR was suggested about 8km. There are many other type of observations for the Venus's great zonal flow and superrotation, e.g. using ground-based Doppler velocimetry measurements of the zonal winds, based on high resolution spectra [P. Machado et al., 2012], however its driving mechanisms are far from the the complete understanding. There are several models to explain this fast atmospheric flow however it still remains a mystery.

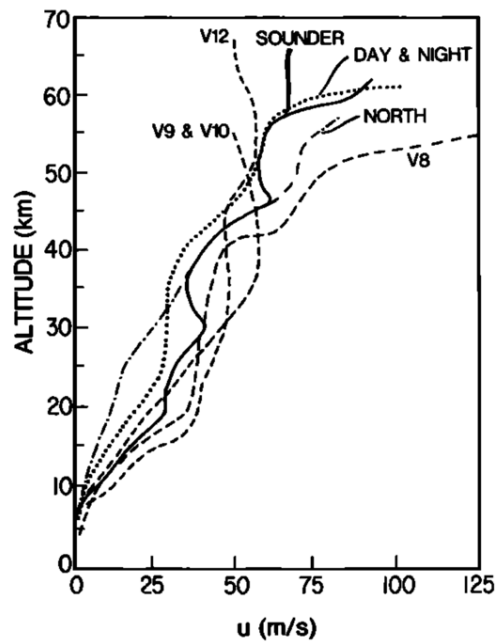


Figure 1.1: Vertical profiles of Venus wind velocity measured by several descending probes. [Schubert, G., et al., 1980]

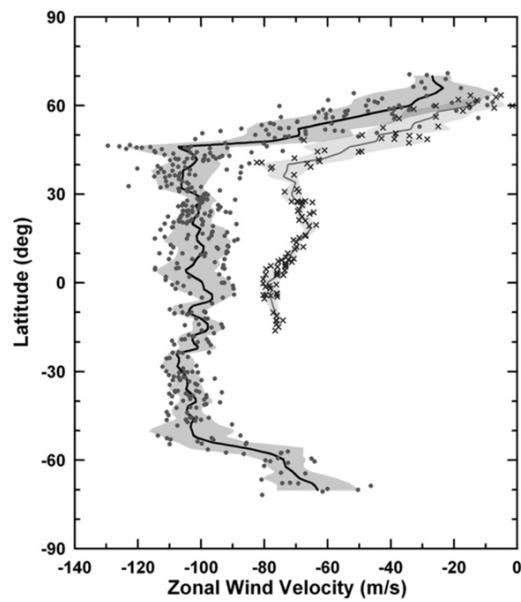


Figure 1.2: Cloud top wind velocities as a function of latitude. [P. Machado et al., 2012]

In general, there are two difficulties to solve the mystery of superrotation. First, Venus's great mean flow is known to have several time scale fluctuation, therefore we need continuous observation for the superrotation. Knowing the time scale of superrotation will help us to find the main source of the atmospheric acceleration. Cloud tracking is one of the best method for monitoring the superrotation. Using satellite images, we can measure the wind velocity with spatial and temporal coverage at some altitudes. Recently, Venus Express, which is the Venus explore of the European Space Agency (ESA), has observed Venus cloud top using UV filter for 8 years. Some thesis reported long-term change of the zonal wind velocity using Venus Express data (e.g. I.V. Khatuntsev et al., 2013; T. Kouyama et al., 2013). Both authors argued that the superrotation accelerated in recent years and additionally in Kouyama et al., (2013) it was suggested that the 255 days long term oscillation exist. Second of the difficulty is that we have less chance to get the vertical profile of Venus atmosphere. The vertical profiles of temperature and pressure are important to investigate the dynamics in the atmosphere for example, How is the meridional circulation in Venus?, Where does atmospheric instability exist and transport the heat flux by thermal convection?, Does vertical propagation of planetary waves exist or not. Radio occultation using a satellite one of the solution to get the vertical information of Venus atmosphere [e.g. Kliore and Patel, 1980]. However it has less spatially resolution for horizontally dimension. For the further investigation about Venus superrotation, we need additional observation, which enable us to monitor the atmosphere with three-dimensional spatial resolution.

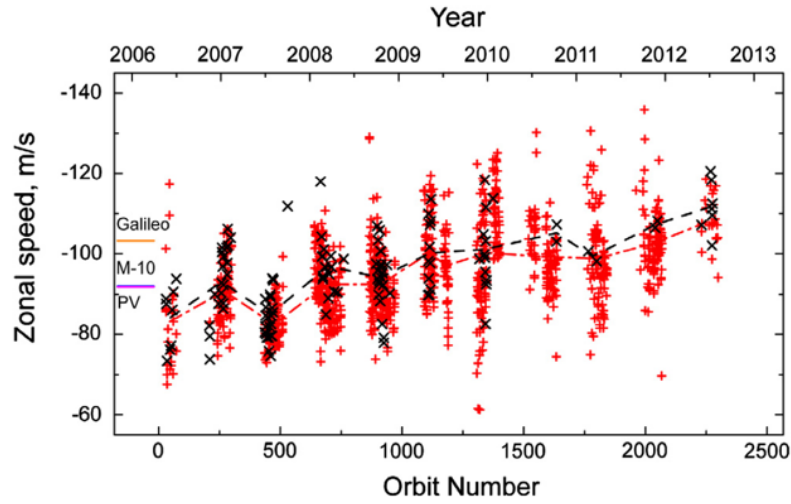


Figure 1.3: Mean zonal wind velocity derived from the cloud tracking using Venus Express observation images. Recently, it can be confirmed that the wind velocity gradually increasing. [Khatuntsev et al., 2013]

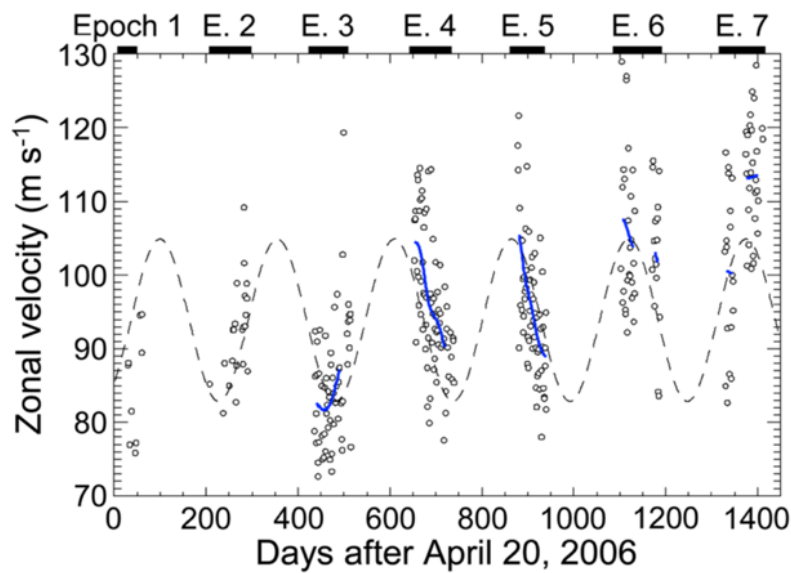


Figure 1.4: From the satellites data, 255 days long term oscillation of the zonal wind velocity also can be observed. [Kouyama et al., 2013]

## 1.2 Y-feature

When we observe Venus in UV range, we can find remarkable features on the disc. Figure 1.5 is the pictures taken by Pioneer Venus. You can notice that there is a large planetary scale feature like letter Y on one's side. Venusian planetary UV feature is empirically known to be observed having high contrast at 365 nm (e.g., Esposito, 1980). The absorbing material is still unknown but it can be one of the markers for monitoring atmospheric motions. These UV features largely regarded to be in cloud top about 65 km however several causes can be considered to make the UV features. Figure 1.6 draws the picture how the dark UV feature is formed. It is reported that the UV absorber rapidly increases below 55 km [Bertaux et al, 1996]. Changing the abundance of UV absorber is one possible reason to make dark pattern. On the other hand, the haze layer is known to exist above the cloud top. In Braak et al, (2001) it was suggested that the cloud top change between 10-25 mbar with their simulation result using data of polarization observation. Therefore the change of the altitude of haze layer top (generally regarded about  $\sim 90$  km) or cloud top should cause the opacity change and make the difference of UV brightness.

Venus Images taken by Galileo using 418 nm and Pioneer Venus using 365 nm are famous because in these images we can find clear Y-feature. Both satellite images cover both hemispheres and Rossow et al., (1980) illustrated the characteristic of UV features from Pioneer Venus images (Figure 1.7). Planetary scale Y-feature propagates about westward and circulates with 4 days period. This periodical circulation can be considered as superrotation and make the UV brightness variation. From here, we focus on the planetary scale UV feature and describe about the formation of Y-feature in detail in the next section.

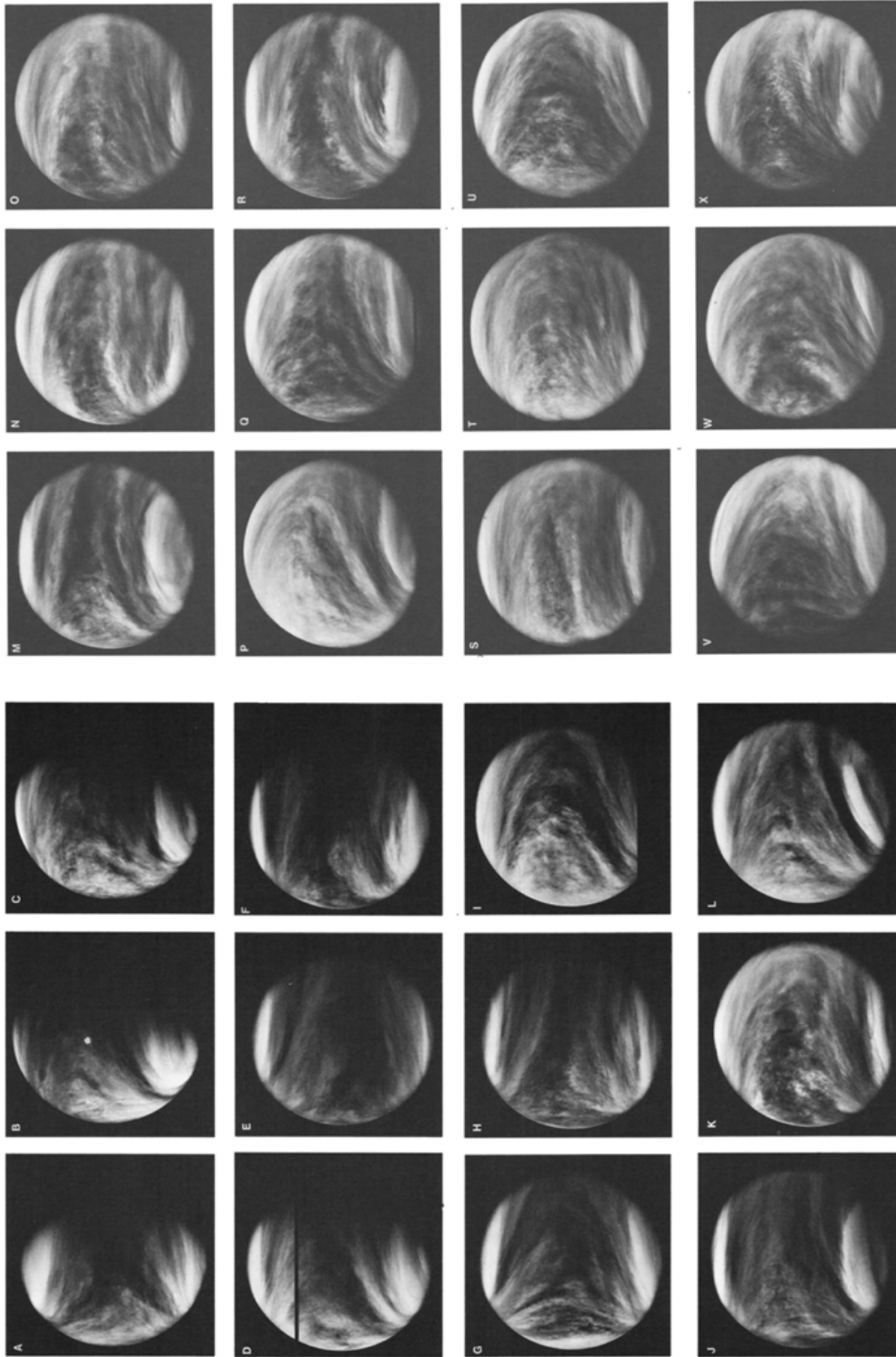


Figure 1.5: UV images of Venus dayside taken by Pioneer Venus. Most of images show the prominent "Y-feature" however it seems have temporal change. [Rossow et al., 1980]

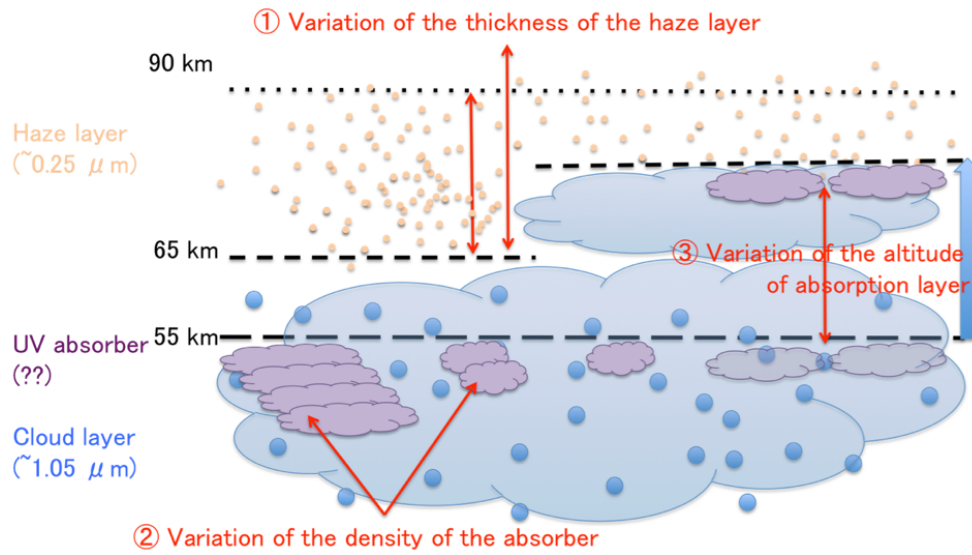


Figure 1.6: Illustration of the cloud top structure and mechanisms of making UV dark feature.

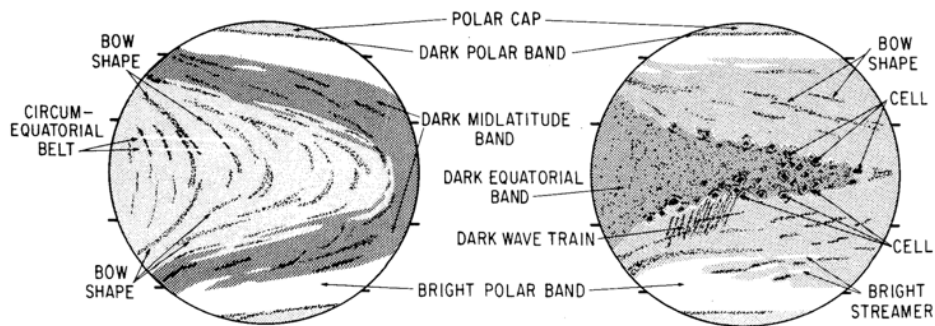


Figure 1.7: Schematic diagram defining the basic types of Y-feature and UV features. This article doesn't mention about the temporal variation of these features in detail. [Rossow et al., 1980]

### 1.3 Atmospheric waves in Venus

Pioneer Venus by NASA is one of the successful exploration for monitoring Venus UV features and superrotation. Orbiter Cloud Photopolarimeter (OCP) is on-board imager of Pioneer Venus with 365 nm filter and it provided us many information about the spatial and temporal distribution of the zonal winds. OCP images are acquired during the long apoapsis portion of the elliptical Pioneer Venus orbit by a spin-scan technique, which requires about 4 hours for the generation of a single full-disc image [Travis, 1979]. A maximum of four full-disk images can be acquired on a single 24-h orbit however the important point is that OCP images cover both northern and southern hemispheres. Usable images can exist no longer than about three months, when the Sun-Venus-Spacecraft phase angle is  $\leq 60^\circ$ . Del Genio and Rossow, (1990) conducted Fourier analysis for the time series of longitudinal mean normalized image brightness and investigate the propagation characteristics for longitudinal wavenumber 1 from spring 1979 to summer 1986. Figure 1.9a, b show the time series of this Fourier analysis results for each latitudes. The propagation of planetary scale UV features caused the periodical variation of UV brightness mostly with the period 4-5 days especially in spring 1979, spring 1980 and spring 1982. In spring 1979, equatorial region had 4-day circulation and mid latitudinal areas in both hemispheres had 5-days. After that the periodicity had changed independently for equatorial and mid-latitudinal areas. Figure 1.10 is further result by Del Genio and Rossow, (1990). They suggest that period of brightness change corresponds to the propagation of planetary wave and compare the period of brightness variation and mean zonal flow which derived from cloud tracking in equatorial region. We can find that the propagation of equatorial planetary wave is correlated with the variations in the cloud level wind speed. They argue that the cloud level atmosphere vacillates between two distinct dynamical states on a time scale of perhaps 5-10 years. In one configuration, planetary-scale equatorial waves and associated slowly moving mid-latitude wave modes are active and equatorial zonal winds are maximum. Over a 2-3 year interval this gives way to an alternative configuration in which equatorial waves are weaker, absent or different in character and equatorial zonal winds are weaker.

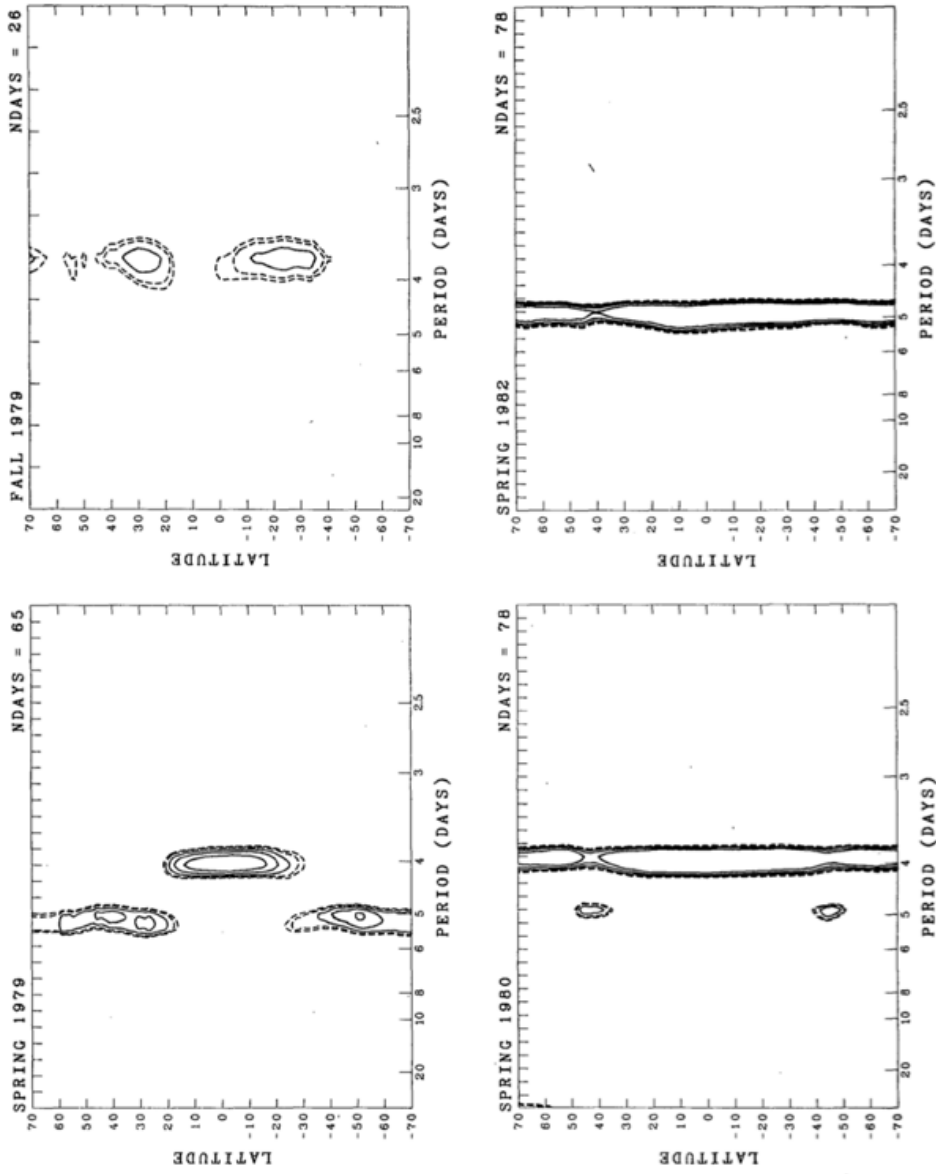


Figure 1.8: Pioneer Venus observe the periodicity of UV brightness variation and found the change of its period. [Del Genio and Rossow, 1990]

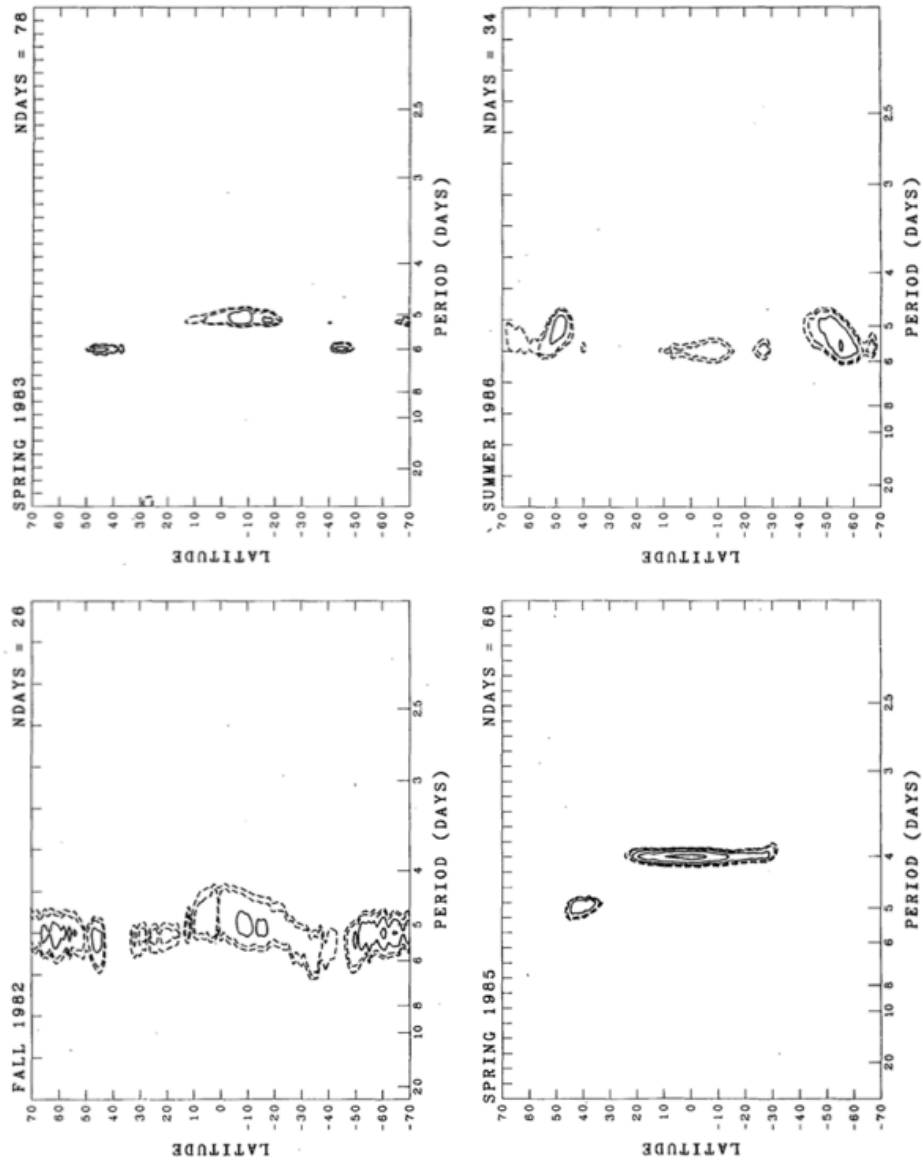


Figure 1-9: Pioneer Venus observe the periodicity of UV brightness variation and found the change of its period. [Del Genio and Rossow, 1990]

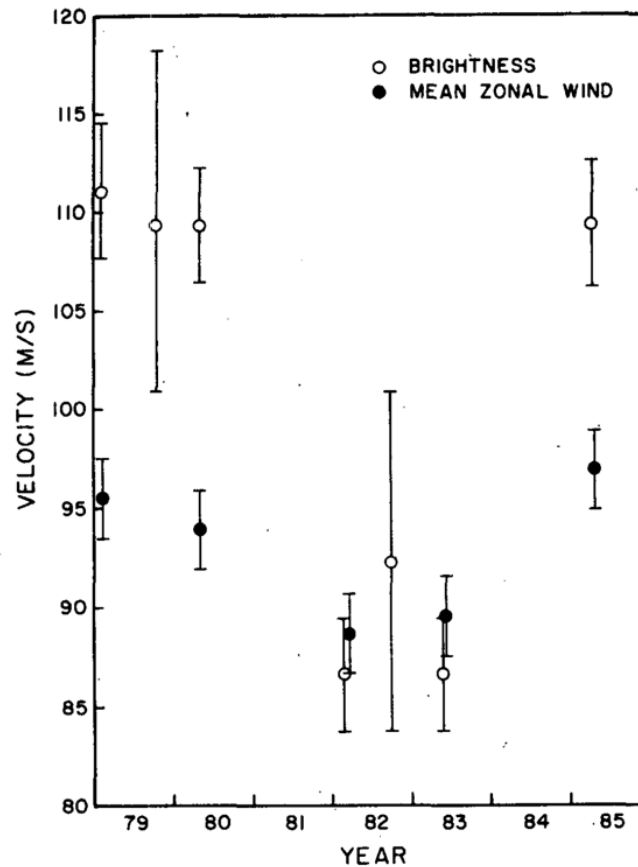


Figure 1.10: Mean equatorial cloud-tracked zonal wind speeds and propagation phase speeds implied by UV brightness periodicity. 5-10 years fluctuation seems to exist. [Del Genio and Rossow, 1990]

After the Pioneer Venus mission, contributions of the planetary waves for the superrotation become to be well considered. Several simulation results suggest planetary scale waves accelerate Venusian atmosphere. Yamamoto and Tanaka (1997a) suggested that the Kelvin wave in equator, which is propagating at an altitude of 70 km or higher, and the Rossby wave in mid-latitude play an important role in the formation of the superrotation (Figure 1.10). They argue that when an appropriate range of the 4-day wave forcing is supplied at the lower boundary of the middle atmosphere, a large zonal-mean flow can be realized from the equator to mid-latitudes. Figure 1.11 is the zonal wind velocity as functions of latitude and altitude from their work. Over the 100 m/s mean zonal flow is reconstructed by their model. Combination of the Kelvin wave and the Rossby wave cause the non-uniform horizontal distribution of eddy geopotential (Figure 1.12). Furthermore, they

found out the distribution of eddy geopotential has a few weeks fluctuation (13.4 days). The time variations of the eddy geopotential at  $60^\circ$  latitude and 62 km height is showed in Figure 1.13.

Their model was applied study is to examine the role that the dynamical transport plays in the global distribution of aerosols. As a result, it was suggested that the effect of the geopotential fluctuation appears as the phenomena of variation of the dark pattern of Y-feature [Yamamoto and Tanaka (1997b)] (Figure 1.14). Results indicate that aerosols, which are considered as UV scatterer of the solar radiation, are accumulated in the polar region due to pole ward transport mainly by meridional circulation (Figure 1.15), and therefore the scattering coefficient becomes higher with increasing latitude. The dark regions in the Y-shaped pattern correspond to the regions with small number density of aerosols at low latitudes. This longitudinal contrast of aerosol concentration is caused by the dynamical combination of the equatorial Kelvin wave and the westward Rossby wave.

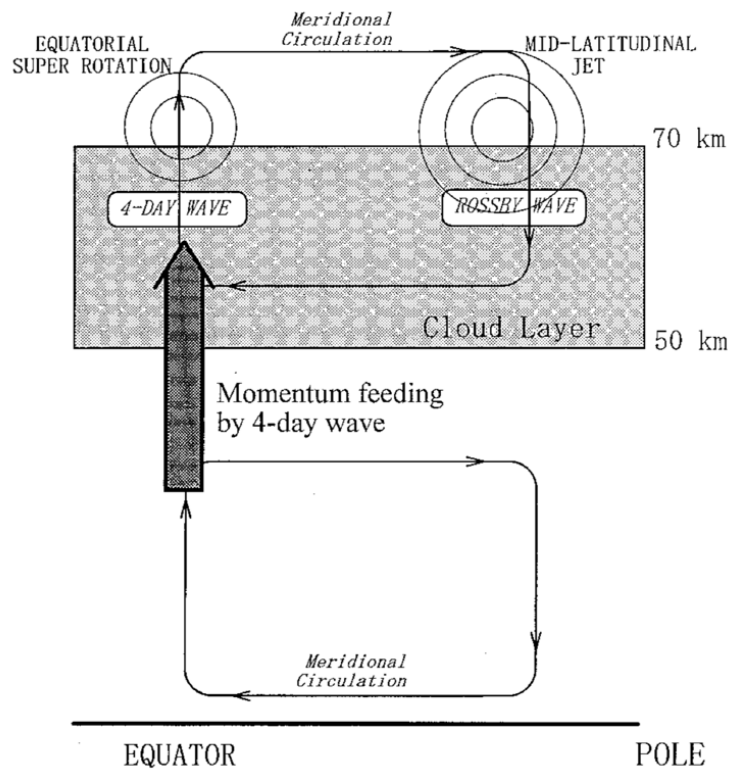


Figure 1.11: General circulation model scheme provided in [Yamamoto and Tanaka (1997a)]. They argue the wave forcing have great contribution to the atmospheric acceleration in Venus.

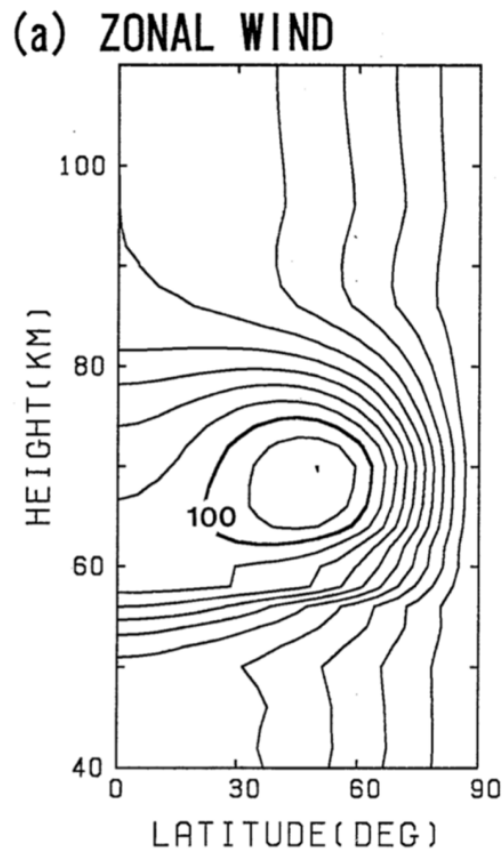


Figure 1.12: Meridional distribution of zonal wind simulated by using the wave forcing model described in Figure 1.10. [Yamamoto and Tanaka (1997a)]

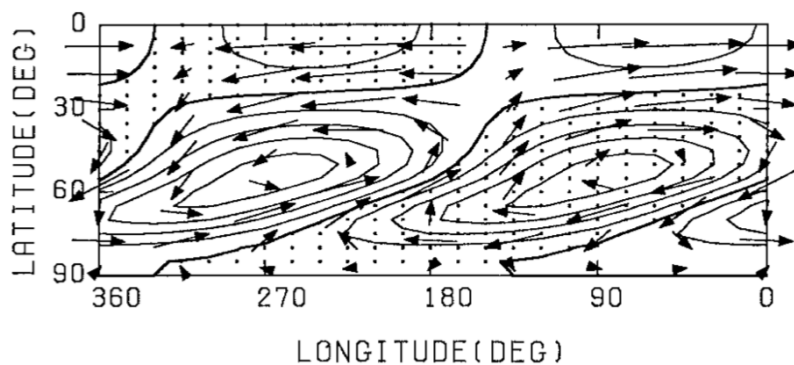


Figure 1.13: Horizontal distribution of eddy geopotential and horizontal flow at 65-km level. [Yamamoto and Tanaka (1997a)]

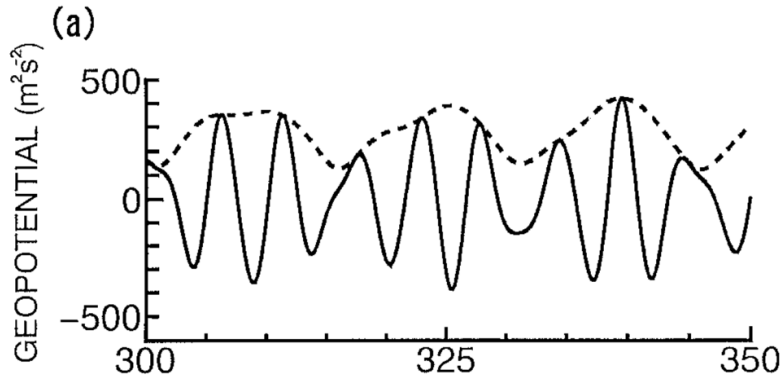


Figure 1.14: Time variations of the eddy geopotential at latitude  $60^\circ$  and height 62 km. [Yamamoto and Tanaka, 1997a]

#### 1.4 Purpose of this study

In the discussion about the cloud level atmosphere vacillates on a time scale of 5-10 years [Del Genio and Rossow 1990], the shorter time scale vacillation are ruled out by the temporal resolution of the OCPP imaging epochs. After the Pioneer Venus mission, there were less further observations to monitor the Venus UV brightness variation for a few months or longer. ESA's Venus Express is on going Venus exploration spacecraft and the Venus Monitoring Camera (VMC) onboard the Venus Express gives us many chances to investigate the variability of UV brightness in Venus. Kouyama et al, (2013) reported that the estimated most significant period of superrotation (mean zonal flow) is about 255 days (also drawn in Figure), that is longer than one Venus year, and thus the oscillation seems to be a non-seasonal cycle.

While at the same time, ground-based observation also has a great potential to monitor the brightness variation. There are several difficulties observing Venus from the Earth such as the change of the phase angle (change the dayside area of Venus), short observable time in night (direction to Venus is near to the Sun), weather condition and Earth's atmospheric extinction. However in respect of the spatial resolution, ground based observation has enough capability to observe the planetary scale features in both hemispheres (e.g. Dollfus et al., 1975) and it is superior at the point of the observation continuity. Venus Express images planetary scale UV features only in southern hemisphere, thus we carried out ground-based observation in the same time period of Venus Express observation.

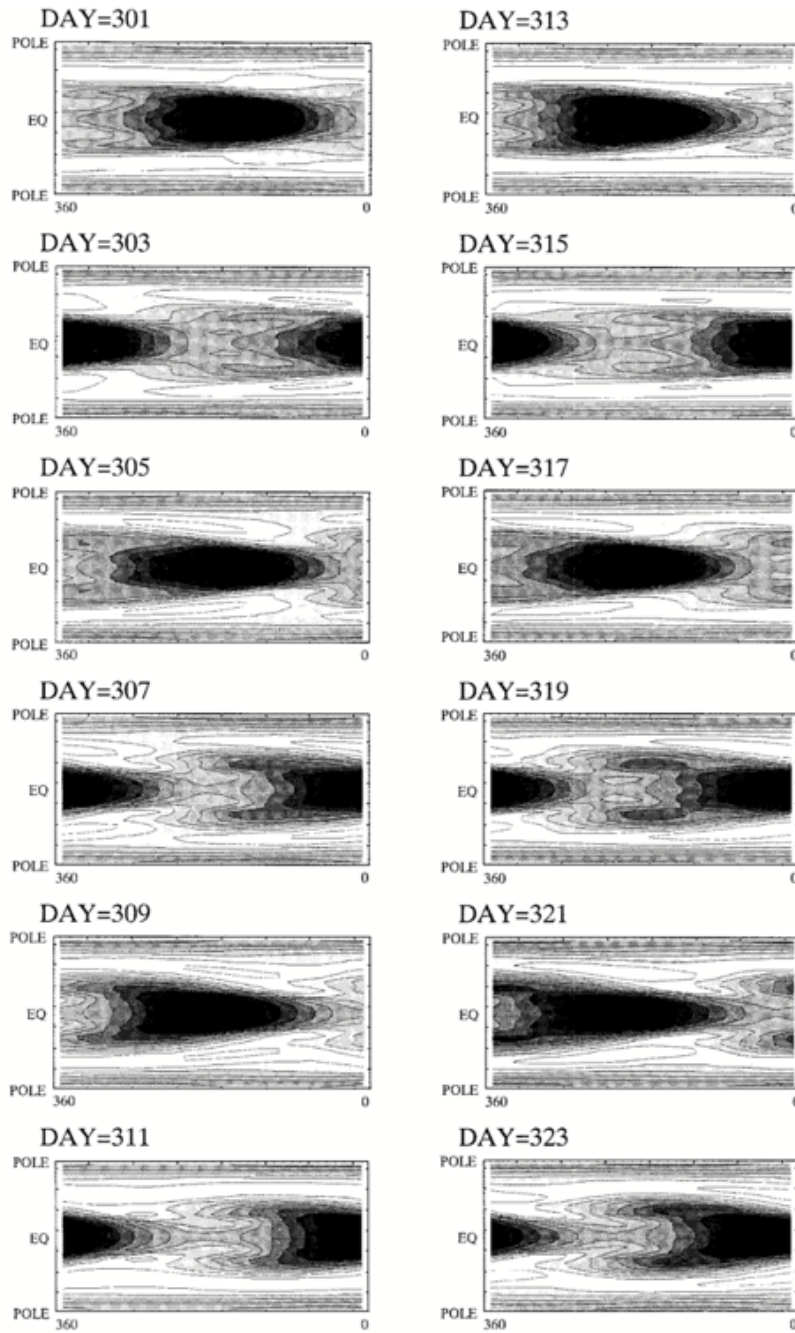


Figure 1.15: Time variation of scattering coefficients at the cloud top altitude. It can be assumed that this kind of variation appear as the pattern of UV feature. [Yamamoto and Tanaka (1997b)]

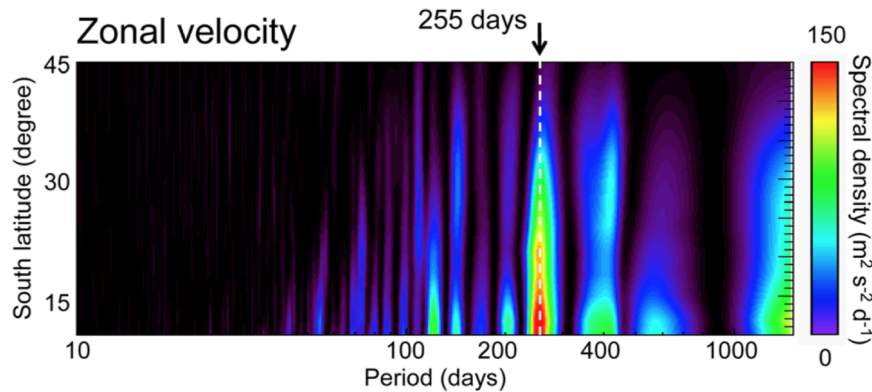


Figure 1.16: Periodical analysis results of the zonal wind velocity as a function of the latitude. 255 days periodical change is the most significant. [Kouyama et al, (2013)]

Here is the brief summary the Introduction.

- Previous Simulation: The coupling of the Kelvin wave (in equator) and the Rossby wave (in mid-latitude) generate a large zonal-mean flow (Super-rotation). Effect of this two planetary waves cause the fluctuation of the geopotential and as a result, planetary scale UV feature is changed.
- Previous Observation: Venus UV brightness varied periodically and this period was changed between 4 and 5 days in a few years however there are not enough observation to resolve the monthly variation of superrotation. Investigating the periodical brightness variation allow us to know the dynamical state of Venus atmosphere.

We consider that planetary waves have great contribution to accelerate Venusian atmosphere, which cause the variability of the Y-feature in a few weeks, however these planetary waves is not seems to have constant power. So the goal of present study is to observe the change of the UV brightness pattern and capture the deformation of Y-feature and estimate the time scale of that change. We regard that the change of the period of UV brightness variation in a few year can be explained by the change of dynamical state (e.g. the planetary Kelvin wave lose the power in a few years). Evaluating and establishing the association between the deformation of Y-feature and the dynamical state of planetary wave will lead to solve the mystery of superrotation.

In Section 2 we describe the information about our ground-based and

the VMC observation, and in Section 3 describe methods of image reduction and analysis. Section 4 gives the results of UV brightness variation. This section also contains the comparison results of our observation and VMC, and discusses the implication about the change of brightness pattern. Section 5 will discuss about our new results and finally Section 6 gives a summary and future work.

## 2 Observation and Data

In this study, we observe the UV feature in Venus disc and monitor the variation of brightness. For the advantage of the observation continuity and coverage of equatorial and both mid-latitudinal region, we decide to use ground-based telescope. Figure 2.1 is the composed image taken by OCPP. From about  $90^{\circ}$ – $255^{\circ}$  longitude, we can find clear Y-feature. Typical scale of the Y-feature is over 20,000 km for zonal direction and about 10,000 km for meridional direction. Venus's angular diameter changes from about 10–60 arcsecond depending on the Earth-Venus distance (Figure 2.2). Our observational requirement is finally derived that Venus angular diameter  $\geq 15$  arcsecond. Observation wavelength is 365 nm which enable us to get high contrast UV feature and same as OCPP and VMC observed.

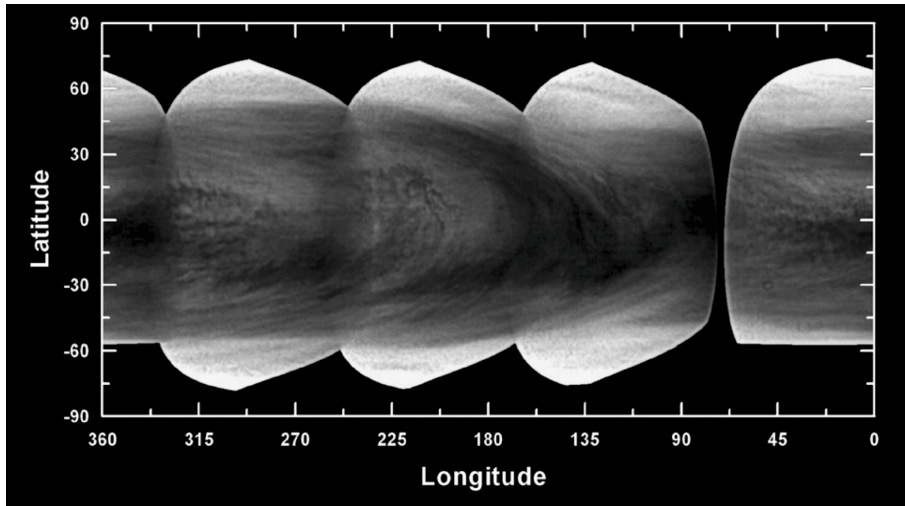


Figure 2.1: Cylindrical projection of a set of Galileo UV images. In near the center of the picture, prominent Y-feature can be seen. [Peralta, J et al., 2007a]

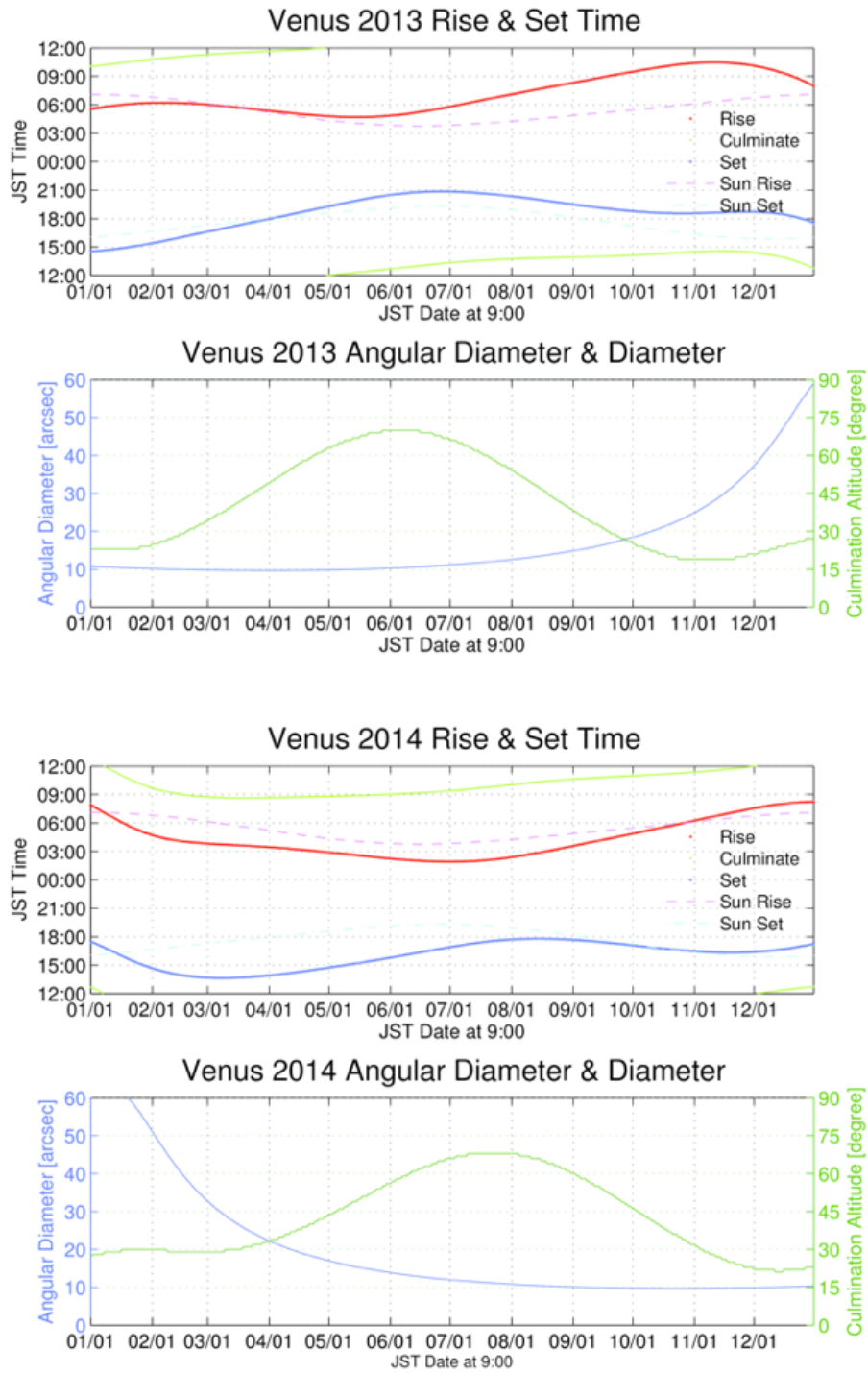


Figure 2.2: Diagram of the Venus almanac in 2013 and 2014 at Nayoro observatory.

## 2.1 Pirka telescope and Multi-Spectral Imager(MSI)

We carried out the ground-based observations with Multi-Spectral Imager (MSI) onboard the "Pirka" telescope [M. Watanabe et al., 2012]. The Pirka 1.6-m telescope is owned and operated by the Planetary and Space Group of the Department of CosmoSciences, the Graduate School of Science in Hokkaido University. Pirka telescope is located at the Nayoro Observatory of the Faculty of Science, the Hokkaido University, in  $145^\circ$  East longitude and  $44.4^\circ$  North at 161 m above sea level. Location site of the Pirka telescope has a good ratio of fine weather and suitable for our monitoring. Typical seeing size is 1.8 arcsec in median and this is enough to observe planetary scale features ( $\geq 10,000$  km). This corresponds to the observational requirement that Venus's angular diameter is bigger than about 15 arcsec to distinguish  $10^\circ$  latitudinal bands. Major specifications of the Pirka telescope is listed below (Table 2.1).

Location coordinate	$44^\circ 22'$ , $142^\circ 28'$ E
Height of observatory	151 m
Optical system design	Ritchey-Chretien
Primary mirror	
- Effective aperture	1600 mm
- Principal focal length	19237.7 mm (F/12.6)
Focal length	
Cassegrain focus	F/12.0
Nasmyth A focus	F/12.0
Nasmyth B focus	F/12.0
Manufacturer	Nishimura Co., Ltd

Table 2.1: Table about the major specifications of the Pirka telescope.

MSI is equipped with a  $512 \times 512$  pixel EMCCD camera, whose frame rate is about 32 Hz (minimum exposure time at our observational mode is 0.035 s using scanspeed2 mode) and its pixel scale is 0.389 arcsec (FOV is  $3.3 \times 3.3$  arcmin). Table 2.2 is the main characteristics of MSI. MSI's EMCCD enables us to obtain Venus images with high background during the daytime observation. Used narrow-band filter has center wavelength at 365 nm and 10 nm bandwidth (Figure 2.3).

Venus sometimes called the morning star or the evening star and after the Moon, it is the brightest natural object reaching an apparent magnitude of -4.6. Because Venus is an inferior planet from Earth, it can't be observed

---



---

Spectral coverage	360–1050 nm
Field of view	151 m
- Resolution	$3.3' \times 3.3'$ (0.389"/pixel)
Filters	
- Liquid crystal tunable filters	CRi VariSpec VIS-10: 400–720 nm, $\Delta\lambda \sim 10$ nm (@ 650 nm) CRi VariSpec SNIR-10: 650–1100 nm, $\Delta\lambda \sim 10$ nm (@ 900 nm)
- Narrow-band filters	360, 365, 370, 380, 390 nm ( $\Delta\lambda = 10$ nm), H $\alpha$ ( $\Delta\lambda = 1$ nm)
- Broad-band filters	Johnson-Cousins U, B, V, R, I
Camera (CCD)	Hamamatsu Photonics C9100-13
Array format	$512 \times 512$ pixel (Pixel size: $16 \times 16 \mu\text{m}$ )
Readout modes	EMCCD mode, Normal CCD mode
Pixel clock rates	11 MHz (EMCCD mode only), 0.69 MHz, 2.75 MHz
Maximum frame rates (full-frame)	31.9 frames/s (EMCCD mode), 2 frames/s (Normal CCD mode)
Minimum exposure times (full-frame)	0.031 s (EMCCD mode), 0.488 s (Normal CCD mode)
EM gain	4 - 1200
CCD cooling method & temperature	Peltier with forced-air, $-65^\circ\text{C}$

---



---

Table 2.2: Table about the major specifications of the Multi Spectral Imager.

at the midnight and also it has a phase like the Moon. We observed Venus in six times from mid-August 2013 to end of June, 2014 (called each observation period OP1–OP6 respectively as Table 2.3). OP3 included the day when Venus was at greatest eastern elongation. We have about three months observation blank around June 2013 because we have inferior conjunction. Before the inferior conjunction, Venus images were taken after when Venus culminated. After the inferior conjunction, we observed Venus before when Venus culminated. Basically our observation was conducted among when the Venus altitude was in  $20^\circ - 90^\circ$ . Maximum observation times were about 8 hours in a day and took images at least thirty images every an hour as the weather was clear. Imaging size is modified to  $512\text{pix} \times 128\text{pix}$  because reducing the number of pixels of Y-direction makes it possible to fast read out. We adopt dithering method when we take Venus images in order to reduce the flat fielding uncertainty. During the twilight time, we took five sky images for making flat frame (twilight flat) and after the observation, dome flat also acquired everyday. Bias images were taken adequately during the whole observation time. Acquiring the photometric standard stars did not conducted because our main observation time was in day time. All data absence in each observation period depends on weather badness.



Figure 2.3: Picture of the 1.6-m Pirka telescope.



Figure 2.4: Picture of the Multi Spectral Imager.

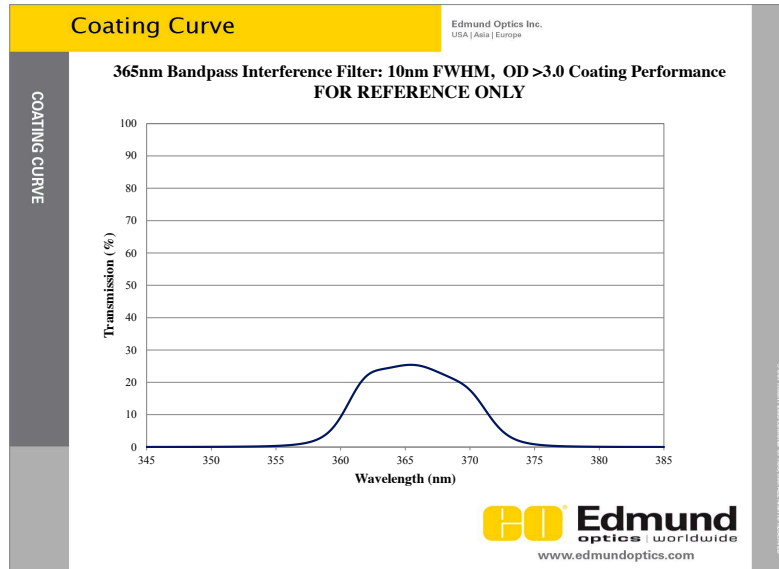


Figure 2.5: Transmission curve of the 365 nm narrowband filter using in this study.

Observation Period	Number of days	Acquisition rate	Diameter [arcsec] ([pix])	S-V-O angle [°]
OP1: Aug 2013 8/19–8/29	10 days	91%	14.1 (36)	58.4
OP2: Sep 2013 9/23–10/8	18 days	71%	18.6 (49)	75.2
OP3: Oct 2013 10/18–11/8	21 days	73%	23.8 (61)	88.2
OP4: Feb 2014 2/25–3/28	31 days	65%	34.7–23.2 (89–60)	109.3–87.5
OP5: May 2014 5/6–6/1	27 days	70%	15.3 (40)	63.8
OP6: June 2014 6/19–6/30	12 days	66%	12.4 (32)	47.8

Table 2.3: Information of our ground-based observation. Acquisition rate means the percentage of success days to take Venus images. From OP1 to OP6 almost cover the one Venus year.

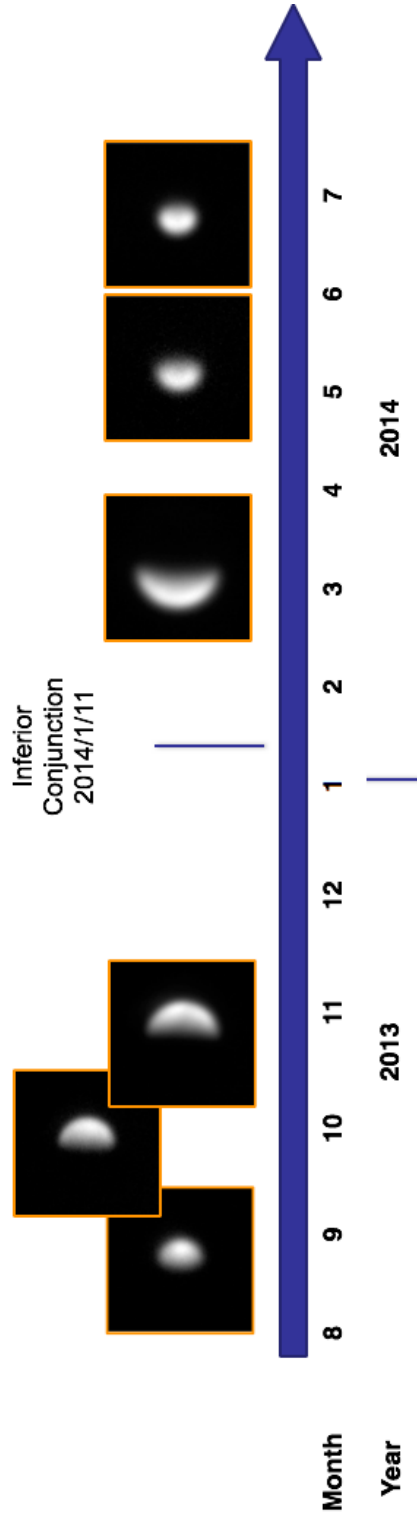


Figure 2.6: Sample images of Venus taken in this study along with the calendar.

## 2.2 Observation from satellites

Venus Monitoring Camera (VMC) onboard Venus Express offers good opportunities to investigate the Venus cloud morphologies (e.g., Titov et al. 2012; Markiewicz et al. 2007) VMC has four narrow band filters and one of its center wavelength is 365 nm (bandwidth is 40 nm). VMC data allow us to estimate the VU brightness variation with no consideration of the Earth's atmospheric extinction. Unfortunately UV features in global scale are captured only in southern hemisphere because Venus Express is in elliptic orbit with a period of 24h and apocenter in southern hemisphere (Figure 2.7). But we can evaluate our ground-based result using VMC data and coupling our MSI's and VMC's data enable us to investigate the Venesian UV brightness variation in both hemisphere. Such approach has never been conducted.

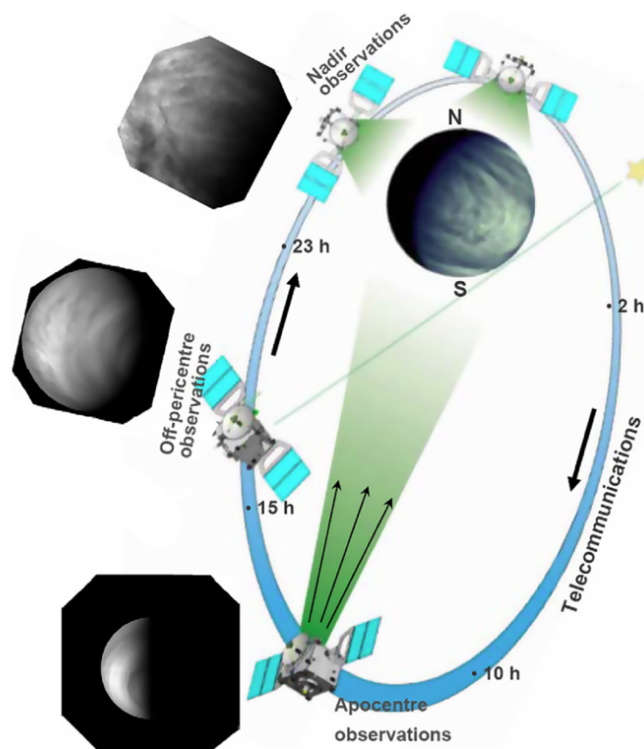


Figure 2.7: Illustration of the Venus Express orbit with sample images. Planetary scale UV features can only be observed in southern hemisphere. [Titov, D. V., et al. ,2012]

### 3 Analysis for ground-based images

#### 3.1 Bias and Flat reduction

Basic CCD image reduction including the subtracting bias frame and dividing by flat field is completed as the following equation.

$$BiasFrame(i, j) = Mean[BiasImage(i, j)]$$

$$FlatFrame(i, j) = \frac{Median[\sum FlatImage(i, j) - BiasFrame(i, j)]}{\frac{1}{MN} \sum_m \sum_n Median[\sum FlatImage(m, n) - BiasFrame(m, n)]}$$

$$ReducedVenusFrame(i, j) = \frac{RawVenusFrame(i, j) - BiasFrame(i, j)}{FlatFrame(i, j) - BiasFrame(i, j)}$$

Here,  $(i, j)$  and  $(m, n)$  mean the X-Y coordinate on the CCD array.  $Frame(i, j)$  represents the Digital Number (CCD counts) of pixel  $(i, j)$ . *Mean* and *Median* are image combining operations. The *Mean* processing strike an average of images and *Median* take a median. Figure 3.1 is the sample raw image of Venus taken on November 1 2013 and Figure 3.2 is same image after the basic reduction.

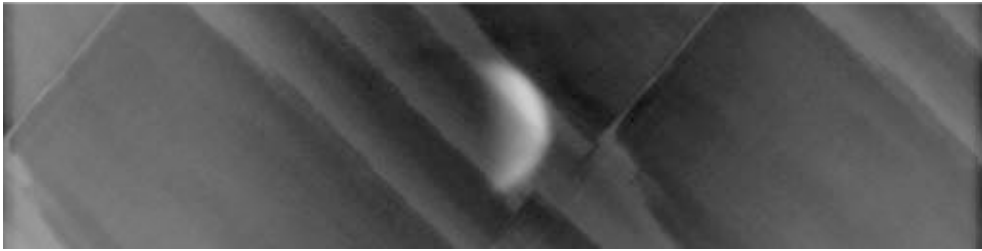


Figure 3.1: Raw Venus image taken by MSI and Pirka telescope in November 1 2013. Some stripe feature is caused by uneven sensitivity of the CCD.



Figure 3.2: Same Venus image as Figure 3.1 but after the basic reduction.

### 3.2 Determination of the Venus geographical coordinates

After the basic reduction process, we need to calculate the geographical coordinates for each pixel of Venus images. Using the geometric information of Venus and the Earth at the observation time, we can make simulated images of Venus. Information is obtained from the JPL's HORIZONS system (<http://ssd.jpl.nasa.gov/?horizons>). The equatorial angular width of the target, apparent planetographic ("geodetic") longitude and latitude (IAU2009 model) of the center of the target disc seen by the observer at a time, apparent planetographic longitude and latitude of the Sun as seen by the observer, north pole position angle (with respect to direction of true-of-date Celestial North Pole) and 1-way light-time from target center to observer is used as parameters of making simulated Venus. Making procedure is described as below.

Using constants is,

*Venus radius* :  $r = 6051.8 + 70$  km

*Pixel scale of MSI* :  $s = 0.389$  arcsec/pixel

Sub-solar longitude and latitude are  $\psi_{Sun}, \theta_{Sun}$ , and sub-observer longitude and latitude are  $\psi_{Obs}, \theta_{Obs}$  respectively (Figure 3.3).

*Vector to the sub-solar point from the center of Venus* :

$$\vec{L}_S = \begin{pmatrix} r \cos \theta_S \cos(\psi_S - \psi_O) \\ r \cos \theta_S \sin(\psi_S - \psi_O) \\ r \sin \theta_S \end{pmatrix} \quad (1)$$

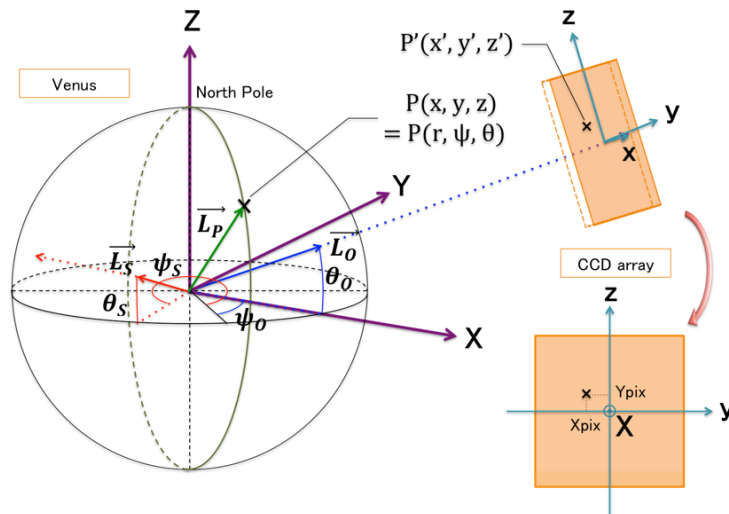


Figure 3.3: A schematic view of the relationship between the Venus geographical coordinates and CCD array.

*Vector to the sub – observer point from the center of Venus :*

$$\vec{L}_O = \begin{pmatrix} r \cos \theta_O \cos(\psi_O - \psi_o) \\ r \cos \theta_O \sin(\psi_O - \psi_o) \\ r \sin \theta_O \end{pmatrix} \quad (2)$$

Next, we fix the center of Venus as origin and set the Cartesian coordinate system (X, Y, Z) of which the x-direction is parallel to an equatorial plane of  $\vec{L}_O$  and z-direction is same direction to the North Pole from the origin.  $\vec{L}_O$  associates with a CCD-array face vertically, and make another Cartesian coordinate (x, y, z) like Figure 3.3. The center of Venus corresponds to the center point of CCD-array, and the xyz coordinate is in the relation of parallel to the one which made the XYZ coordinate rotate  $\theta_{Obs}$  about Y-axis.

Now, we seek the point on Venus where corresponds to the pixels on CCD-array. A point on CCD ( $X_{pix}$ ,  $Y_{pix}$ ) can be set in a xyz coordinate system from the following equation.

$$y' = k X_{pix} \quad (3)$$

$$z' = k Y_{pix} \quad (4)$$

$$x' = \sqrt{R^2 - y'^2 - z'^2} \quad (5)$$

now  $x > 0$ .

Constant k is,

$$k = \frac{R s}{60 \cdot 60 \cdot 180 \cdot \pi}. \quad (6)$$

R is the distance from Venus to the Earth derived using the 1-way light-time (from HORIZONS). According the above processing, we can set the point P' on CCD to the ( $x'$ ,  $y'$ ,  $z'$ ) coordinate.

Transformation of the point P''( $x'$ ,  $y'$ ,  $z'$ ) to the P( $x$ ,  $y$ ,  $z$ ) is as follow.

$$\vec{L}_P = \begin{pmatrix} x \\ y \\ z \end{pmatrix} = \begin{pmatrix} \cos \theta_O x' - \sin \theta_O z' \\ y' \\ \sin \theta_O x' + \cos \theta_O z' \end{pmatrix} \quad (7)$$

Next step is to determining the center pixel of Venus in images. In order to calculate right longitude and latitude in each pixel, we need to know where is the center of Venus. In this process, we make simulated image of Venus and then estimate the center by superimposing the actual image and this simulated image. Simulated Venus images are also made by using equations (1), (2) and (7). For the simple case, Lambert surface whose surface is illuminated isotropically can be assumed. However by our trial analysis we found that the actual image and simulated image are quite different. In Belton et al. [1991], they use Irvine's ground-based photometry data, with phase-angle dependence, to calibrate the brightnesses in images. These images are taken with 418 nm band but we confirm the improvement of simulated image. Therefore we decided to use their empirical function:

$$I = \frac{F_s}{\pi\mu} (\mu\mu_s)^k \frac{1 - \exp(-\mu_s/a)}{1 - \exp(\mu/b)} \quad (8)$$

Here,  $I$  is the reflected intensity and  $F_s$  is the solar flux,  $\mu_s$  is cosine of the solar incidence angle (measured from vertical) and  $\mu$  cosine of the emission angle. Constants are  $a=0.0547$ ;  $b=0.0039$ ;  $k=0.9$ ; following [Belton et al., 1991]. In our analysis,  $\mu_s$  and  $\mu$  can be derived from equation (9) and (10). Equation (9) simulate the appearance of Venus as s sphere when we see Venus from the Earth. Sub-observer point equal to 1 (Figure 3.4). Equation (10) has same form and represent the sun illumination gradient (Figure 3.5). Lambert surface brightness can be estimated by multiplying (9) by (10) (equation (11) and Figure 3.6). Figure 3.7 is the Belton's simulated image. We can easily notice that the there are great difference between Lambert and Belton's. And Belton's simulated image is seems to be more similar to the actual image (coopering Figure 3.2 and 3.7).

$$\frac{\vec{L}_P \cdot \vec{L}_O}{|\vec{L}_P||\vec{L}_O|} \quad (9)$$

$$\frac{\vec{L}_P \cdot \vec{L}_S}{|\vec{L}_P||\vec{L}_S|} \quad (10)$$

$$B_{Lmb} = \frac{\vec{L}_P \cdot \vec{L}_O}{|\vec{L}_P| \cdot |\vec{L}_O|} \quad (11)$$

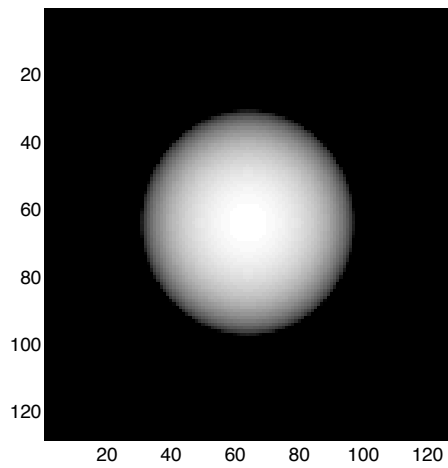


Figure 3.4: Venus simulated sphere observed from the Earth.

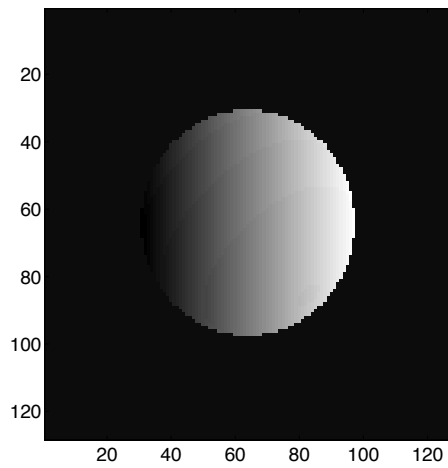


Figure 3.5: Simulated Venus sphere illuminated by Sun.

After the calculation of the Belton's equation (8), we have to concern about the "seeing effect". Disturbance of the Earth's atmosphere, temperature gradient and so on cause the refraction of light and images of astronomical objects become blurring. So our simulated images also include this effect. After some trial, we decided to use Gaussian filter to reconstruct the blurring simulated images. Details of our Gaussian filter are below.

Filter size =  $31 \times 31$  Assumed seeing size : 3.3 [arcsec] (constant)  
 FWHM = seeing / 0.389 [pix]  
 Standard deviation =  $\text{GFWHM} / (2 \cdot \sqrt{2 \cdot \log(2)})$

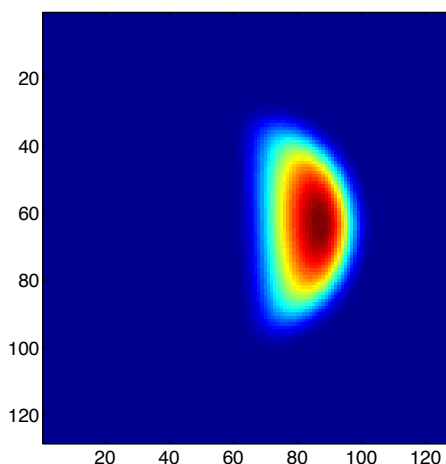


Figure 3.6: Lambert surface simulated image.

Figure 3.8 shows the filtered Belton's simulated image.

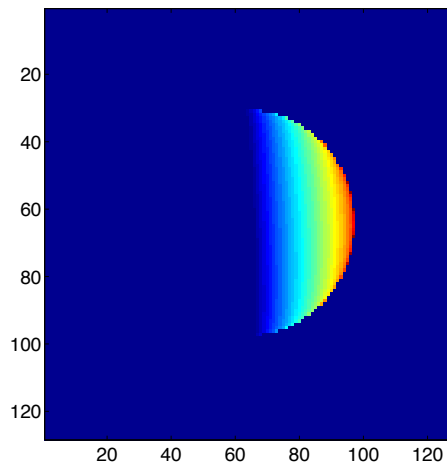


Figure 3.7: Belton's simulated image.

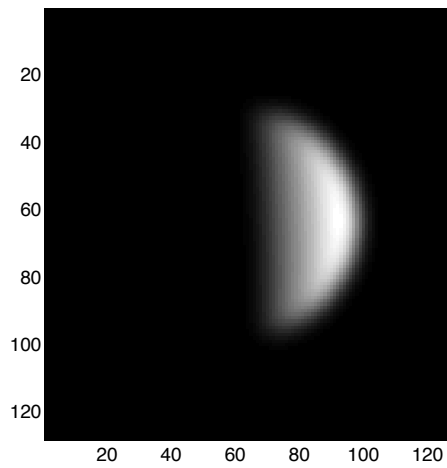


Figure 3.8: Final simulated image applying Gaussian filter to Belton's image.

Simulated Venus image has the axis of rotation same direction with the Y-axis of the image. So after rotating simulated image (rotation amount is the value of north pole position angle from HORIZONS), we determine the center of Venus by using both actual and simulated images. In this process, we calculate the cross-correlation coefficient. If the pixel of the center of Venus in a actual image exactly correspond to that of simulated image, the cross-correlation coefficient become the highest. For the calculation of cross-correlation, we use two dimensional fast Fourier transformation (FFT). Here,  $f(x, y)$  and  $g(x, y)$  are actual image and simulated image respectively. After the FFT,

$$f(x, y) \xrightarrow{FFT} F(u, v), \quad g(x, y) \xrightarrow{FFT} G(u, v)$$

we calculate cross-spectral  $S(u, v)$  as below. Here,  $G^*$  represent the complex conjugate of  $G(u, v)$ .

$$S(u, v) = F \cdot G^*$$

And then, cross-correlation coefficient  $C(x', y')$  is calculated after the inverse Fourier transformation (IFFT).

$$S(u, v) \xrightarrow{IFFT} C(x', y').$$

Since  $x'$  and  $y'$  represent the amount of displacement, we can estimate the center pixel of Venus in the actual image.

After that, by transforming the equation (7), we can finally calculate the longitude and latitude of a location  $P(x, y, z)$  on the Venus cloud top (assume the height  $\sim 70$  km) for each pixel. Sample of the calculated result is displayed in Figure 3.7, 3.8. Note that all of the images Figure 3.4-3.8 are adjusted that the center of Venus become the center of images.

$$\text{Longitude} : \psi = \psi_{Obs} + \sin^{-1}(y/r \cos \theta) \tag{12}$$

$$\text{Latitude} : \theta = \theta_{Obs} + \sin^{-1}(z/r) \tag{13}$$

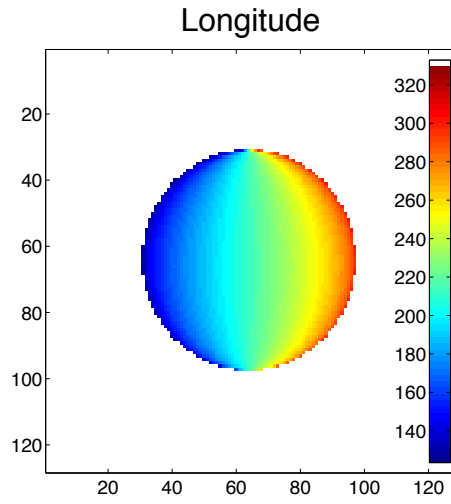


Figure 3.9: Image of the calculated longitude.

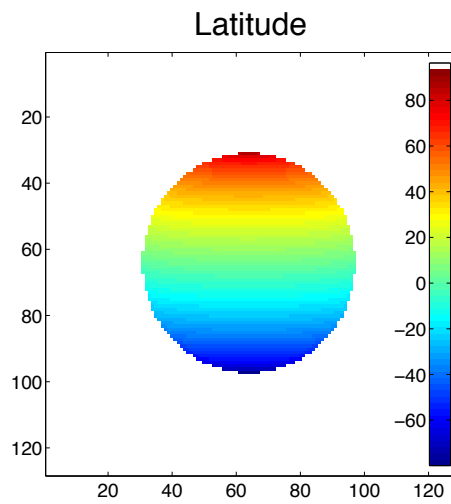


Figure 3.10: Image of the calculated latitude.

### 3.3 Determination discrepancies of Venus geographical coordinates

In this subsection, the determination discrepancy of the Venus geographical coordinates is discussed. The possible main component bringing the matching error between actual image and simulated image is seeing effect. As described above, we fix the seeing value 3 arcsecond to make Gaussian filter (Figure 3.8). So if the actual image was experienced much larger seeing effect, the determination discrepancy thought to being worse. Therefore we conduct the test analysis to evaluate our method.

For this test analysis, we choose three observation days listed in Table 3.1. Venus in these three days have different size of angular diameter, and more than 100 images were taken in a day. Several Gaussian filtered images are made for this analysis (set the seeing size from 2 to 8 arcsecond in a random manner) and we run through the matching process 5 times for all images. Figure 3.11-3.13 are the results of test analysis. The horizontal axis is the setting seeing size and the vertical axis is amount of displacement (pixel) of miss matching for each X and Y direction. As a result, there is no dependency on the seeing size and we can find there are less miss determination. Most of the matching process (over 95%) has less  $\pm 1$  error and rare of them is more. In the Table 3.1, the percentage for each displacement value is listed. In conclusion, our simulated image have negligible error for determining the discrepancy of geographical coordinates. Differences of the final calculated brightness value caused by discrepancies of the geographical coordinates determination are summarized in Appendix A.

Acquired date of the sample	Angular diameter [arcsec]	Discrepancy		
		$\pm 0$	$\pm 1$	$\pm\sqrt{2}$
August 22 2013	14.0	92.8%	5.3%	1.1%
October 6 2013	19.3	91.1%	7.6%	0.7%
November 1 2013	25.0	92.3%	4.8%	1.6%

Table 3.1: Results of the test analysis for the determination discrepancies of Venus geographical coordinates.

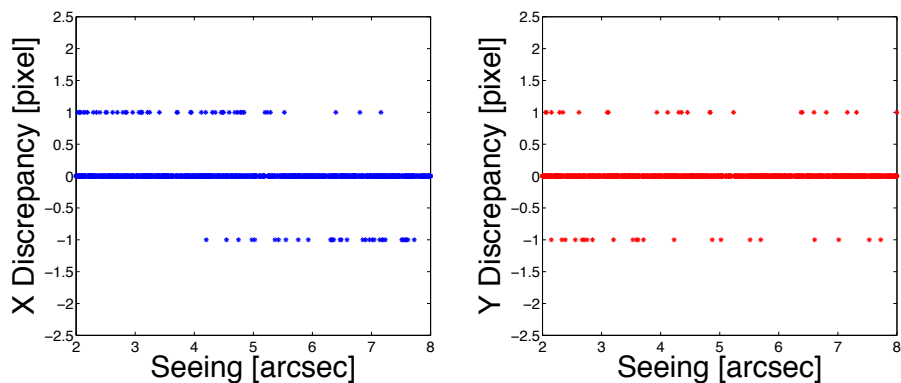


Figure 3.11: Seeing dependence of discrepancies of the geographical coordinates determination for each direction (X and Y) with August 22, 2013 data.

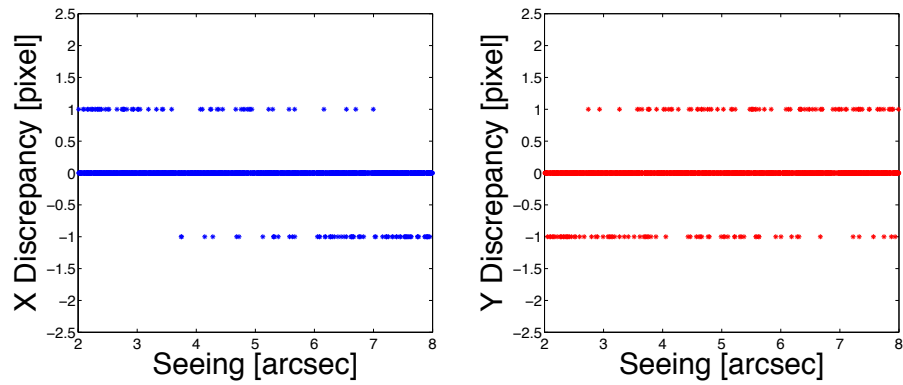


Figure 3.12: Seeing dependence of discrepancies of the geographical coordinates determination for each direction (X and Y) with October 6, 2013 data.

Figure 3.13: Seeing dependence of discrepancies of the geographical coordinates determination for each direction (X and Y) with November 1, 2013 data.

### 3.4 Evaluate the seeing effect

In general, astronomical point sources can give us information about the seeing size in the field of view on that observation time. However most of our observation time is in daytime and we have less chance to take star images. Venus is not a area light source (not a point source) and it is difficult to estimate the seeing size. After next subsection, we will discuss about the measurement of brightness and study about it's variation. In order to avoid rebuttal that point out the contribution of seeing effect for our obtained brightness variation, now we need to make some standard to evaluate the seeing size for each Venus images.

For the sake of evaluating seeing effect, we calculate the ratio of total CCD counts in the area of simulated Venus image over total counts of actual Venus image. Former of simulated Venus image is provided as already described which have't been included Gaussian filtering process (for example Figure 3.7). Latter of total counts of actual Venus image is calculated using pixels within two times radius of Venus from the center. Figure 3.14 shows the summing area of actual image for that case of image taken in November 1 2013. Back ground is subtracted rightly (mentioned in next subsection). When the seeing size is larger, actual Venus image become more expanded and therefore the calculated ratio become smaller. We consider this ratio as the seeing evaluation value (SEV) and calculate the value for all Venus images. Figure 3.16 and 3.17 are the results of the time variation of this value. Red dashed lines represent the  $\pm 1$  standard deviation. To exclude the contamination of seeing effect to the results of brightness variation, we will analyze only images whose SEVs are located between red dashed lines.

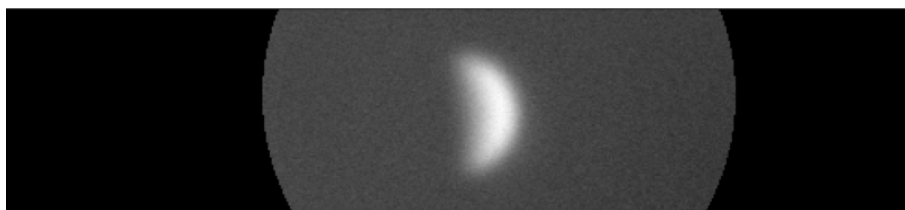


Figure 3.14: Display sky areas within two times radius of Venus from the center area for the calculation of the SEV.

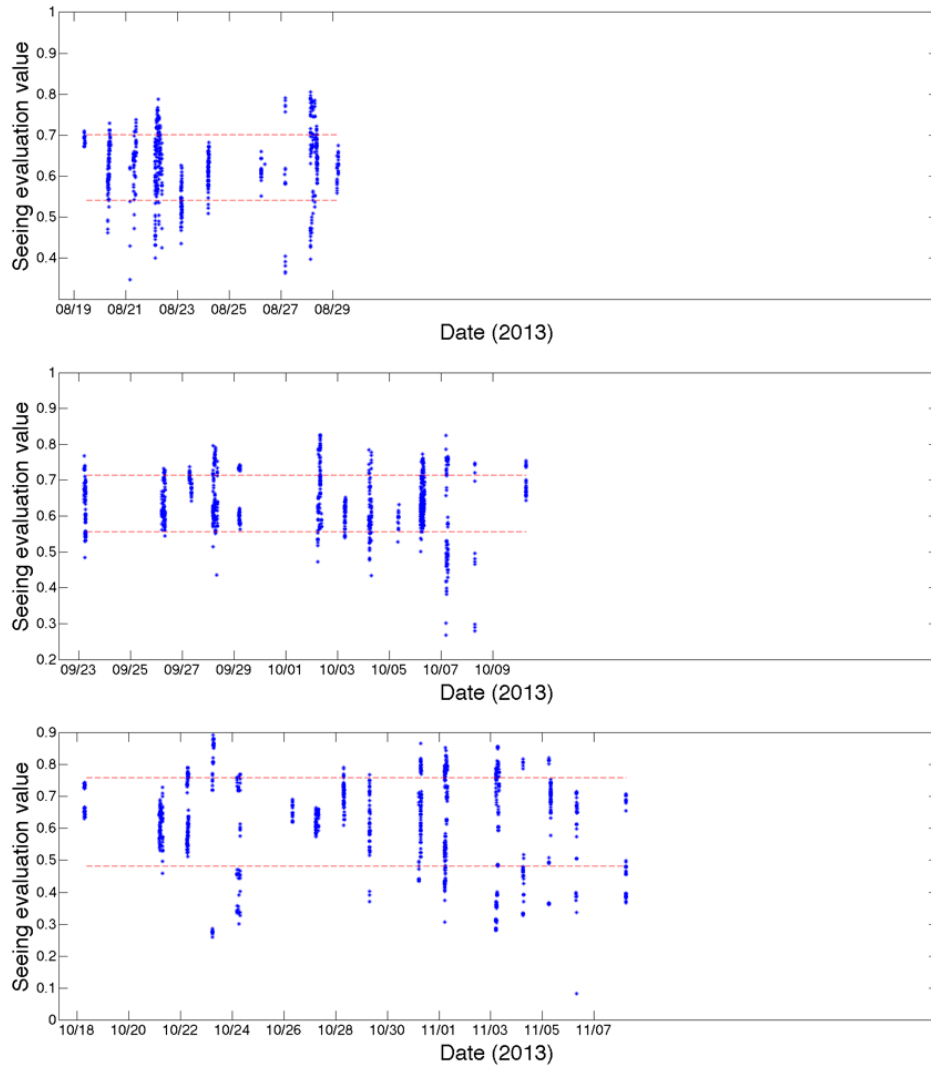


Figure 3.15: Plot of the SEV for all images in OP1-3. Images in between two red dashed lines are used for brightness measurement.

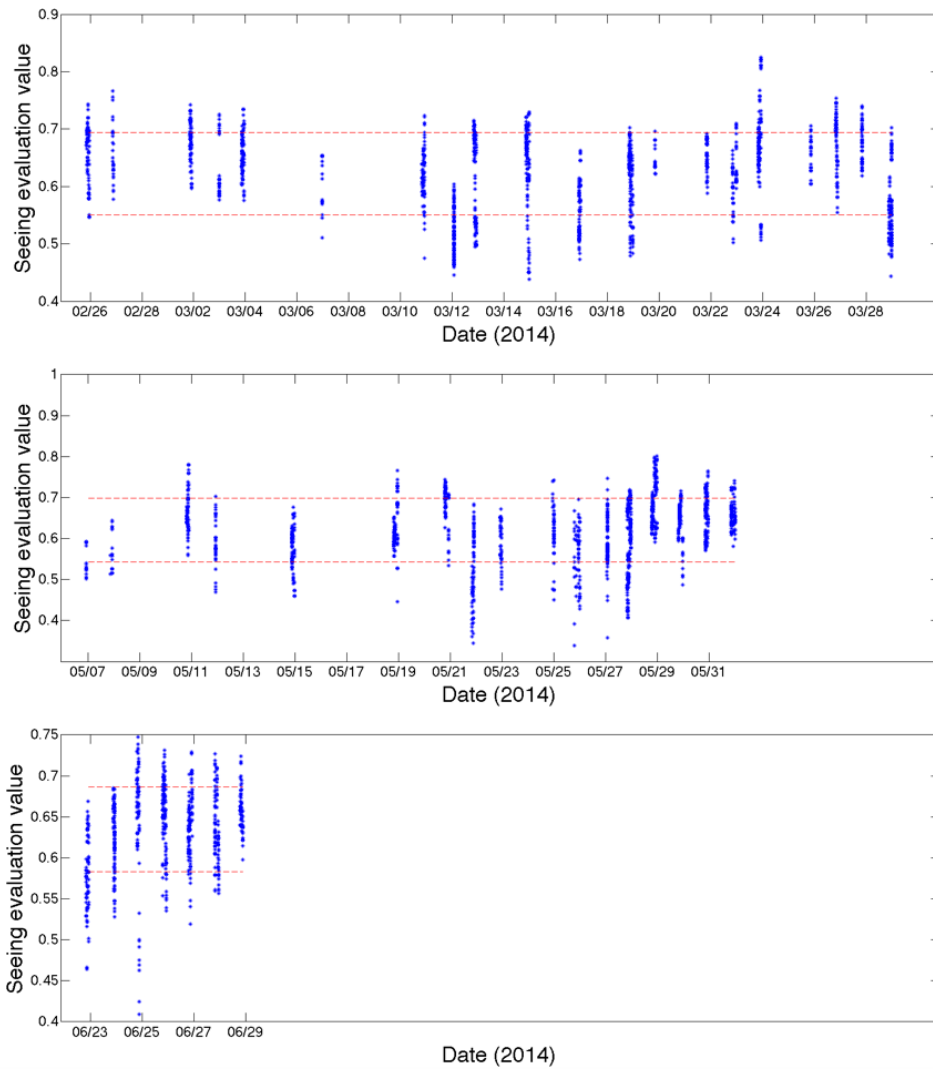


Figure 3.16: Same diagram with Figure 3.15 for images in OP4-6.

### 3.5 Methods to subtract extinction effect of the Earth's atmosphere and measure the brightness variation

Before the brightness measurement, we must subtract the sky background counts. Sky background was estimated using pixels of sky region which was apart two times radius of Venus from the center and subtracted. (Figure 3.17) Some images were taken in midday and background noise becomes higher. Therefore the sky background dominate the signal to noise ratio (SN ratio) and in this study we choose images (SN ratio  $> 10$ ) for the purpose of measuring more than 10% brightness variation (Belton et al. 1991). They reported the 25% fluctuation was exist in 418 nm from Galileo observation and empirically 365 nm is known to have larger contrast in near UV range. And also we select out images in analysis when the standard deviation of sky background ADU count is less than 2 times square root of mean sky background count in order to eliminate images that affected by slight clouds.



Figure 3.17: Display sky areas used for the calculation of sky background.

After the subtraction of sky background, we measure the brightness at each latitudinal band in Venus. The size of extract region is  $60^\circ \times 10^\circ$  (longitude  $\times$  latitude). We determine the center longitude of the region is just middle point of sub solar longitude and sub observer (Earth) longitude in Venus dayside. Center of latitudinal bands are set at  $0^\circ$ ,  $\pm 10^\circ$ ,  $\pm 20^\circ$ ,  $\pm 30^\circ$ ,  $\pm 40^\circ$ ,  $\pm 50^\circ$ ,  $\pm 60^\circ$ . The geometry of each Venus image is estimated using the longitude and latitude simulated image like Figure 3.7, 3.8.

We need to calibrate the atmospheric extinction effect of the Earth's atmosphere to measure the brightness variation. In general, this calibration needs to observe photometric standard stars however there were some difficulties to image Venus and stars simultaneously. The main reasons are strong scattering at 365 nm by the atmosphere of the Earth, and high airmass or bright background. To investigate the brightness variation, we perform a simplification procedure for each image that we normalize the brightness in each latitudinal band with the mean brightness in  $65^\circ\text{N}$ - $65^\circ\text{S}$  area (as the

equation (14),  $\theta$   $\theta'$  represent the each latitudinal bands) and get the disc relative brightness. By this procedure, we cancel out the difference of extinction intensity among images. We conclude that this procedure makes less artificial variation by comparing with VMC data. We will discuss in detail about this in Section 4.

$$R(\theta, day) = B(\theta, day) / \sum_{\theta'} B(\theta', day) \tag{14}$$

Final results of relative brightness values from all images taken in one observation days are averaged and its typical standard deviations are 0.05 at  $0^\circ$  and 0.16 at  $\pm 50^\circ$ . After the averaging, these values in each latitudinal band are linearly "detrended" with respect to its arithmetic average through a least-squares fit and to be set it's mean value equal to 1. Figure 3.18–3.20 represent the example of detrending procedure for  $50^\circ\text{N}$ ,  $0^\circ$ ,  $50^\circ\text{S}$  in OP1. This mean subtraction allows us to notice easy which latitudinal bands have more obvious bright variation.

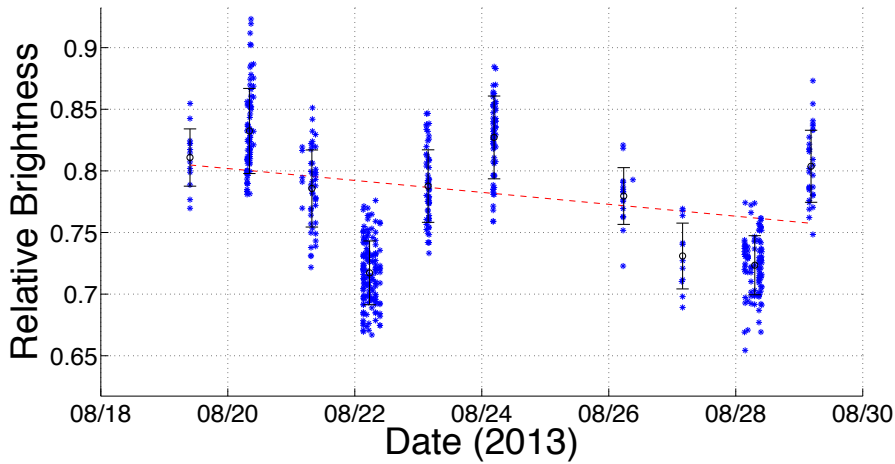


Figure 3.18: Display the detrended process for data from OP1 in  $50^\circ\text{N}$ . Red dashed line shows the linear fitted base line.

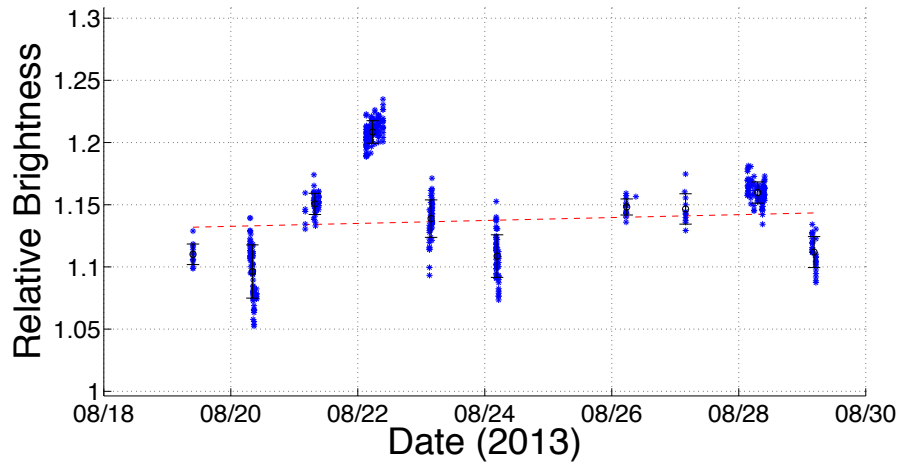


Figure 3.19: Display the detrended process for data from OP1 in  $0^\circ$ . Red dashed line shows the linear fitted base line.

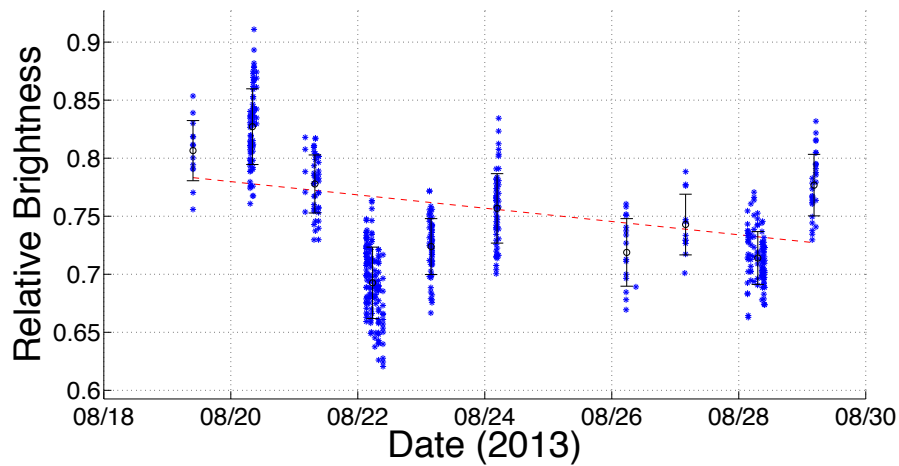


Figure 3.20: Display the detrended process for data from OP1 in  $50^\circ\text{S}$ . Red dashed line shows the linear fitted base line.

### 3.6 Test analysis for the Galileo images

Testing our calibration procedure used for MSI images, we analyze another Venus UV images, which the Solid State Imaging system (SSI) on-board Galileo spacecraft took. SSI had a 418 nm violet filter and it got images shortly after the Venus flyby for 5 days (Used images described in Appendix B). Compositing five Galileo images clearly shows the dark Y-features (Figure 3.21A). Horizontal axis is a relative longitude and we can find large Y-feature between  $150^\circ$  and  $400^\circ$ . Figure 3.21B is the result adopting the calibration procedure described in Section 3.1 for Galileo images. Horizontal axis is time instead of relative longitude and red color shows brighter areas and blue color shows darker areas. From this result, we concluded that the existence and the propagation of large Y-feature showed a prominent structure having four characters that; (1) the cycle of bright and dark pattern exist in equatorial and both northern and southern mid-latitudes, (2) bright and dark pattern has inverse relation between equatorial and mid-latitudes regions and (3) brightness in northern and southern mid-latitudinal areas are synchronized and its distribution is symmetry about the equator. In the following section, we regard this prominent structure is caused by High contrast Y-feature and call it as "HY-feature".

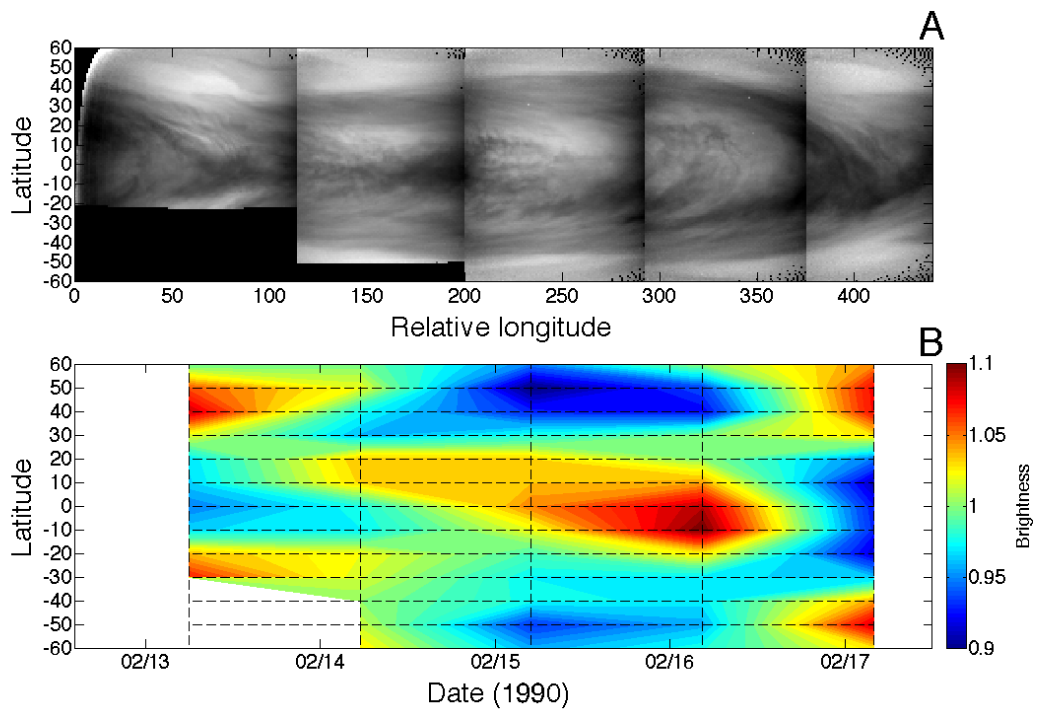


Figure 3.21: Test analysis result for the Galileo observation data. Upper window (A) is the composed Galileo violet images and downer window (B) shows the brightness variation adopting our calibration procedure for ground-based observation images.

## 4 Results

### 4.1 Comparison of the brightness variation between MSI and VMC

Our reduction processes (described in previous section) had some possibilities to make some artificial brightness variation. To confirm MSI's results are valid and not unnatural variation, we compare the MSI's brightness variation with VMC's between 20°S and 60°S where the southern mid-latitude wave has strong amplitude. Explanation about the VMC observation is described in section 2.3 and VMC data is acquired from the ESA's data server (<ftp://psa.esac.esa.int/pub/mirror/VENUS-EXPRESS/VMC>). VMC's simultaneous observation data exists in OP1-3 and we can investigate the UV brightness variation in the area between latitudes 20°S and 80°S. Used images are listed in Appendix C with the information of sub-solar points and sub-satellite points on Venus. The longitudinal size of extraction area is 60° that is same as the MSI's and center longitude of area equal to sub solar longitude. We set the latitudinal size 5° and make latitudinal bands every 5° from 20°S to 80°S. VMC data has no extinction effect from the earth atmosphere and in this study we just only use the brightness (counts of VMC images) with no additional calibration. Original procedure for VMC images are described in Titov et al. (2012) and geometries are determined applying Ogohara et al. (2012). Some images are still strongly affected by hot pixels or dark pattern but this time we neglect them. Brightness in VMC images has strong dependence in the position of Venus Express satellite (especially incident angle of sun light, emission angle from the cloud top and phase angle). So basically we choose images in condition that the sub satellite latitude was within 75°S-85°S and satellite at ascending arc of the orbit (at the dayside of Venus). In this limiting condition, we used one image of Venus southern hemisphere in a day.

Comparison results are shown in Figure 4.1-4.3. Upper window shows the MSI's and lower shows VMC's brightness variation as functions of observation day and latitude. Overlapping areas are marked using bold black dashed lines and they show the comparable data between MSI and VMC. We can find good correlation in both results. Note that there are local time differences of observing area between MSI and VMC because the center longitude of MSI's extraction area is just middle point of sub solar longitude and sub observer longitude, on the other hand VMC's one is sub solar longitude. Maximum difference of longitude is about 1 day (if we estimate the period of wave propagation is 5 days). The minimum longitudinal difference is 28.2° in

August 19, 2013 and maximum is  $47.5^\circ$  in November 8 2013. VMC's brightness values are also linearly detrended by the same way as MSI's in each latitudinal band. Comparing between upper and bottom windows in each figure 2-4 with the consideration for the local lime difference, we can find similarities between MSI's and VMC's brightness variation. Especially, the periodical bright and dark cycle in observation period 1 and smaller brightness distribution from October 18 to November 1 in observation period 3 are reconstructed quite similar. In some date, the absolute value of brightness in MSI's have some tendency to become lower. This effect will be discussed in section 5.2. In our conclusion, we consider the analytic artificial component is less than the inherent brightness variation after comparing our observation data with VMC data.

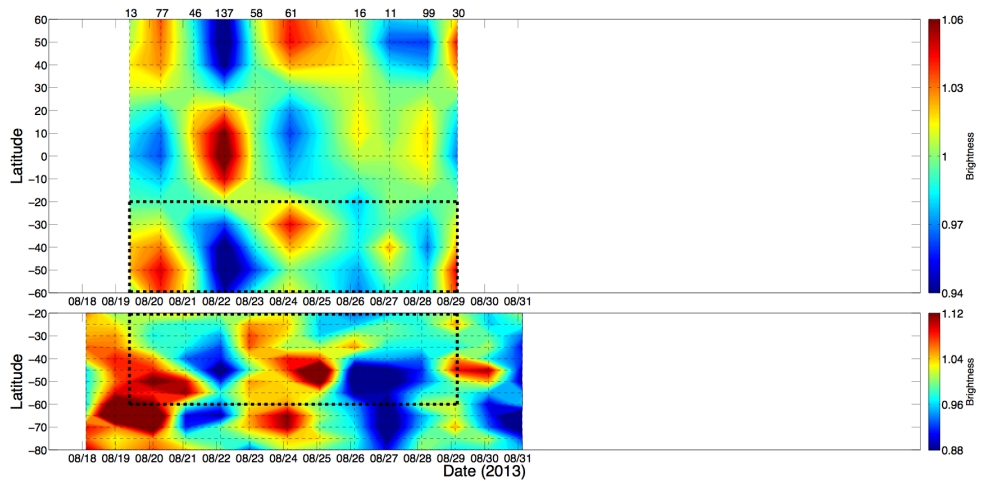


Figure 4.1: Result of the brightness variation as functions of latitudes and observation days for OP1. Downer window shows same diagram with comparable VMC data (for southern hemisphere.)

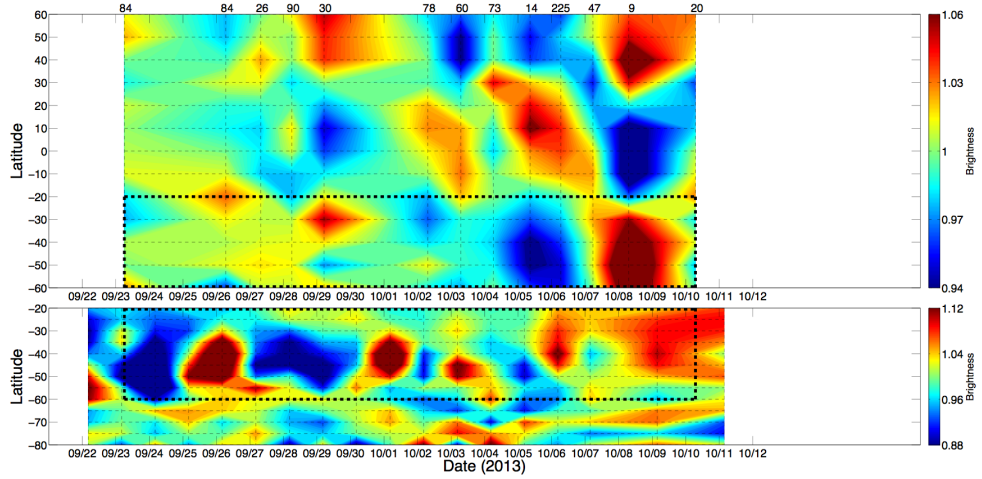


Figure 4.2: Result of the brightness variation as functions of latitudes and observation days for OP2. Downer window shows same diagram with comparable VMC data (for southern hemisphere.)

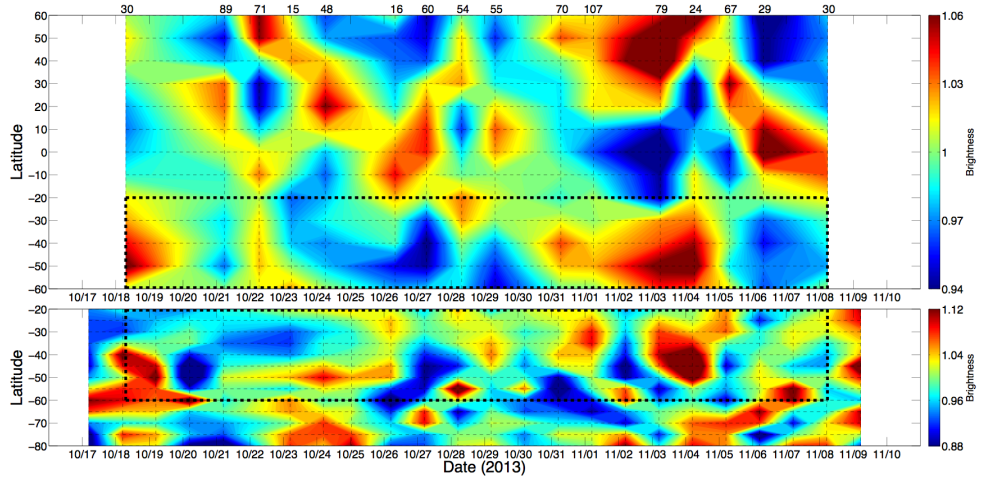


Figure 4.3: Result of the brightness variation as functions of latitudes and observation days for OP3. Downer window shows same diagram with comparable VMC data (for southern hemisphere.)

## 4.2 Fluctuation of UV features

After the analysis (Section 3), we get the results about the time variation of the UV brightness. Note that the brightness of MSI' data means normalized brightness value. Figure 4.4-4.9 shows the variation of UV brightness as functions of latitude and time. Results for OP1-3 are same as Figure 4.1-4.3 upper window and white covered place means data lack. MSI's data cover the latitudes from 60°N to 60°S. Grid lines (dashed lines) show the data existence and the numbers on the top of figures means the number of images in use. Observation was carried out every day but there are some missing data because of the bad weather. Linear interpolation is adopted to fill the missing data and make color contour.

From results of our six observational period, we detect the dynamical change of brightness distribution structure. Our data shows we have two seasons when the brightness has the periodical variation. In August 2013 (Figure 4.4), we detected about 5 days periodical brightness changes in equatorial and both northern and southern mid-latitudinal region. Bright and dark pattern had a prominent periodical and symmetric structure about the equator and we consider it is derived from a high contrast Y-feature such as previously observed by the Galileo spacecraft. On the other hand, after the mid-September 2013 (Figure 4.5, 4.6), there was no prominent and periodical brightness variation in the most of the observation time. In this season, all of these periodical and symmetric brightness structure maintain only for 1-1.5 phase (5-7 days) and they have cycles of being clear and unclear. Especially around 8/19-8/24, 10/5-10/10 and 11/3-11/8, we can find Galileo like Y-features clearly. We suppose that it suggests the Y-feature is not always dominant. The absence of the periodical variation seems to continue by the end of March 2014. In the last two months (from the beginning of May to the end of June 2014, Figure 4.8, 4.9), however, it has less than 4 days period and perhaps last for about two months.

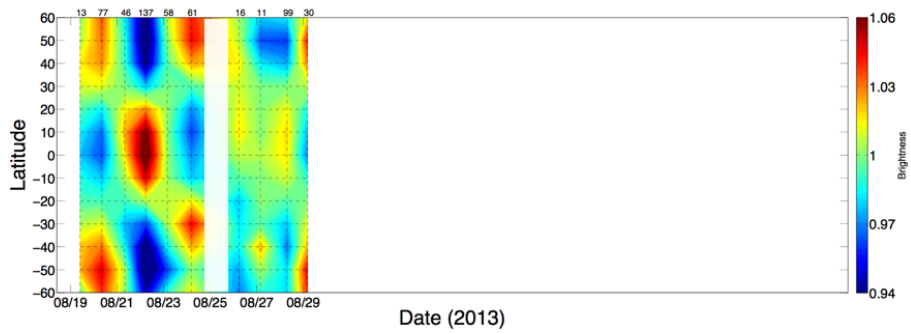


Figure 4.4: Results of the brightness variation as functions of latitudes and observation days for OP1. White bands shows the data lack in that day.

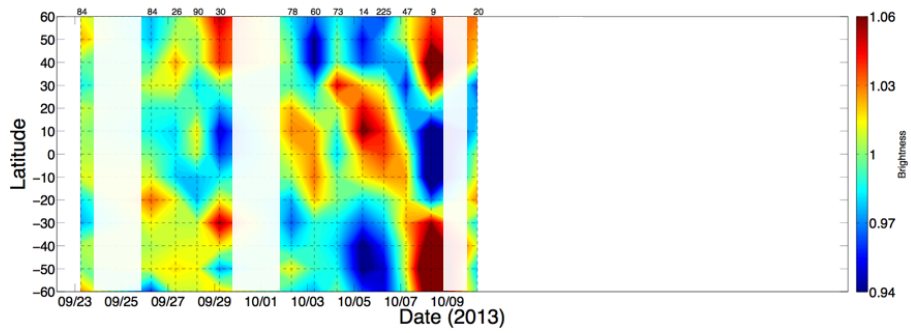


Figure 4.5: Results of the brightness variation as functions of latitudes and observation days for OP2. White bands shows the data lack in that day.

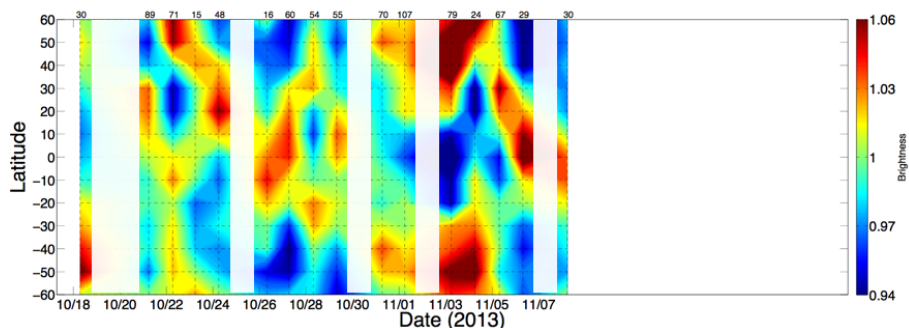


Figure 4.6: Results of the brightness variation as functions of latitudes and observation days for OP3. White bands shows the data lack in that day.

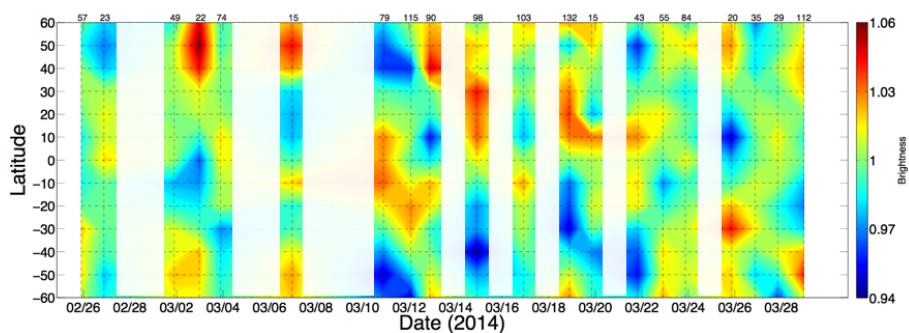


Figure 4.7: Results of the brightness variation as functions of latitudes and observation days for OP4. White bands shows the data lack in that day.

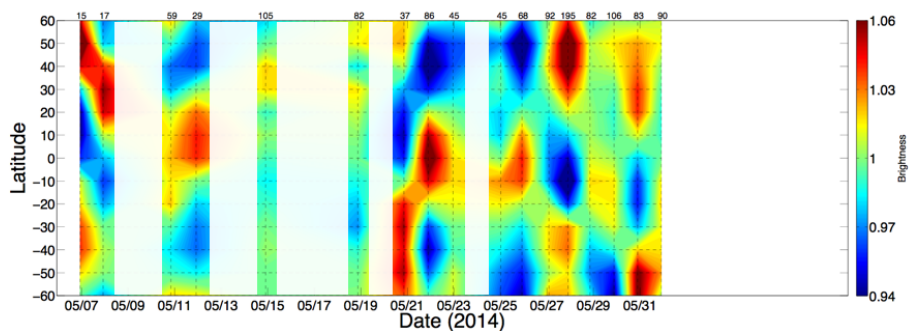


Figure 4.8: Results of the brightness variation as functions of latitudes and observation days for OP5. White bands shows the data lack in that day.



Figure 4.9: Results of the brightness variation as functions of latitudes and observation days for OP6. White bands shows the data lack in that day.

### 4.3 Periodicity of the UV brightness variation

Here we discuss about the periodical UV brightness variation in detail. The periodicity UV brightness variation in our data is studied using Lomb-Scargle periodogram [Lomb, 1976; Scargle, 1982]. This analysis allows us to obtain the power spectra from unevenly sampled data and this method is equivalent to least-squares method fitting the sinusoidal waves to the data. (Appendix D)

We average out the UV brightness data from  $10^{\circ}\text{N}$  to  $10^{\circ}\text{S}$ . Figure 4.10-4.15 show the results for each observation period. Horizontal axes are Period from 0 to 30 days and vertical axes are spectral power. Three horizontal lines in the middle part of diagram shows the significance level for 99%, 90% and 50 % respectively. We mainly focused on the first and second peak periods between 3.0 - 7.0 days. The previous observation data from Pioneer Venus has the period in a range from about 3.9 - 6.0 days [Del Genio and Rossow, 1990]. Some of our data have about 10 days spectrum peaks and they will be discussed briefly later. Results of periodic analysis about the first significant period also summarized in Table. From our analysis, we have three observational period when the brightness variation have prominent periodicity (OP1, OP5 and OP6). In August 2013 (Figure 4.10), the spectrum has a peak power at 5.2 days. On the other hand, in May and June 2014 (Figure 4.14, 4.15), the spectrum peaks are in about 3.5 days. And also, OP5 and OP6 have almost same period but the power is decrease in OP6. In September 2013 (OP2, Figure 4.11) seems have 4.5 days period however a little fast about 3.5 days period also exist. As well in October 2013 (OP3, Figure 4.12) has two peaks at 5.5 days and 3.5 days. However, in February 2014 (OP4, Figure 4.13) when the middle season between OP1 and OP5,

there is no significant periodicity. So a brief summary of our observation is that the periodicity in UV brightness variation is 5.2 days in August 2013 and after 9 months the period changed to 3.5 days.

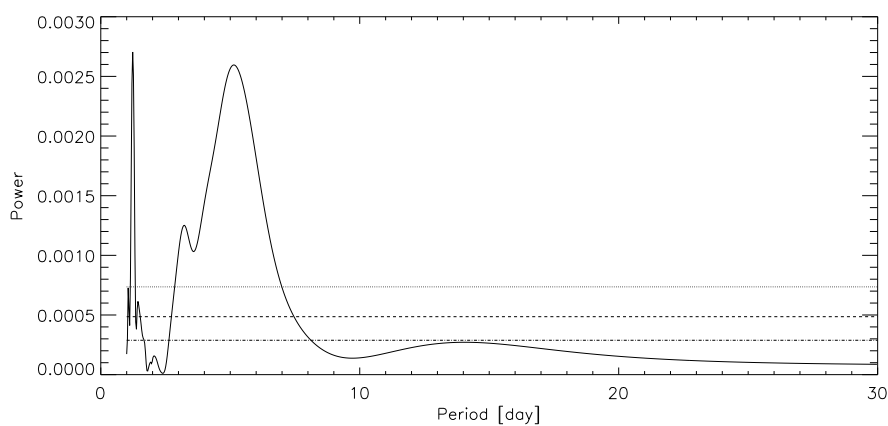


Figure 4.10: Power spectra derived from Lomb-Scargle periodgram with data in OP1.

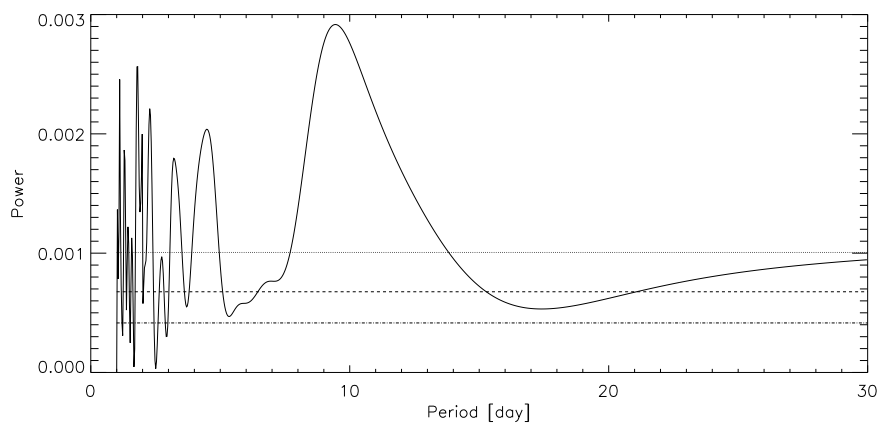


Figure 4.11: Power spectra derived from Lomb-Scargle periodgram with data in OP2.

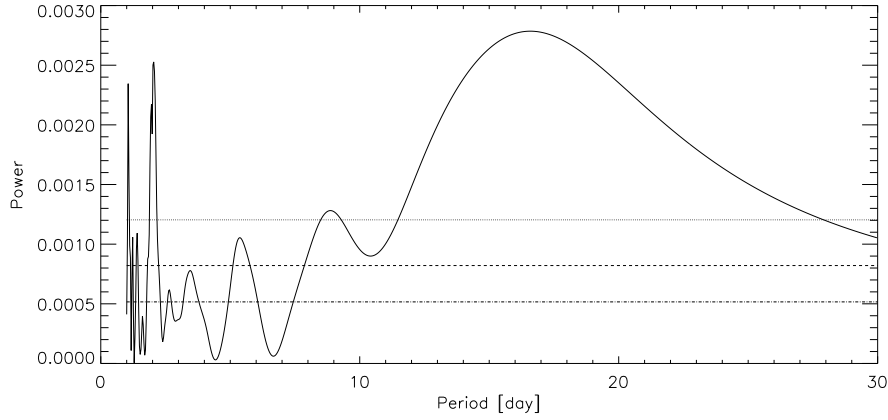


Figure 4.12: Power spectra derived from Lomb-Scargle periodogram with data in OP3.

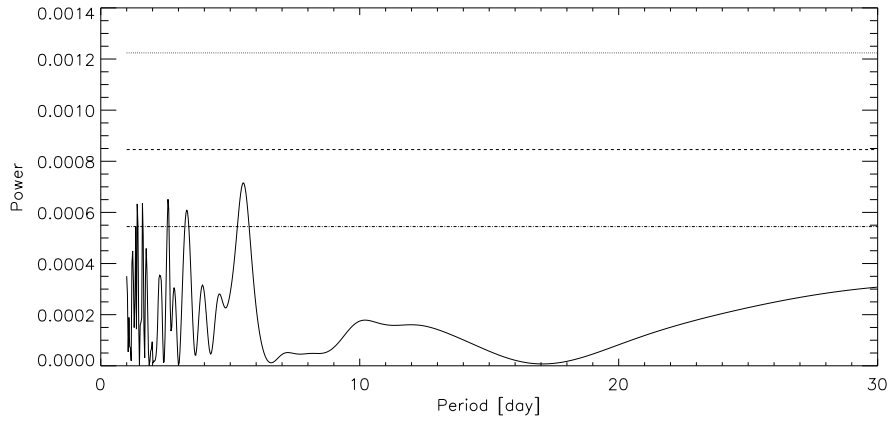


Figure 4.13: Power spectra derived from Lomb-Scargle periodogram with data in OP4.

	Period [day]	Power
OP1 (Aug 2013)	5.15	0.0026
OP2 (Sep 2013)	4.48	0.0020
OP3 (Oct 2013)	5.37	0.0010
OP4 (Feb 2014)	-	-
OP5 (May 2014)	3.49	0.0033
OP6 (June 2014)	3.49	0.0024

Table 4.1: Significant period and it's power calculated from Lomb-Scargle periodogram with our observational results.

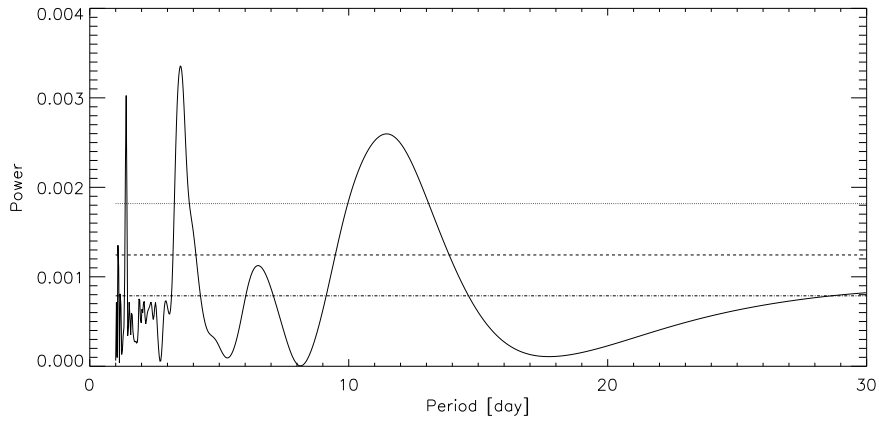


Figure 4.14: Power spectra derived from Lomb-Scargle periodgram with data in OP5.

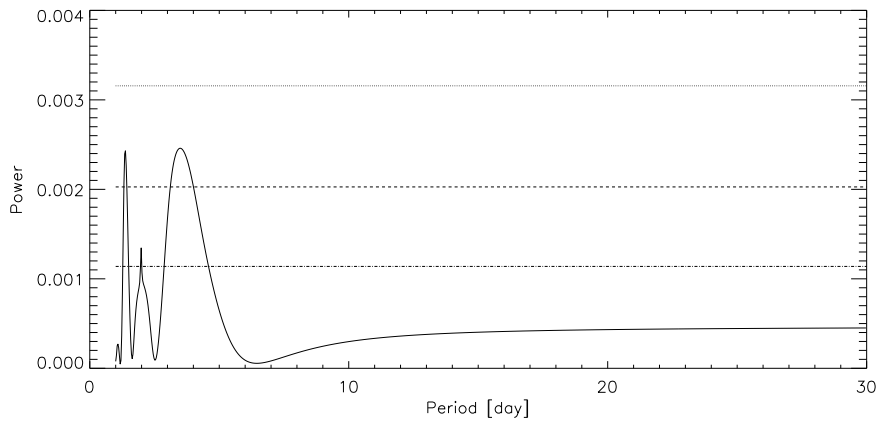


Figure 4.15: Power spectra derived from Lomb-Scargle periodgram with data in OP6.

## 5 Discussion

At first, we discuss about the time scale of the periodicity change. Our observations clearly show that the period of UV brightness variation change 5.2 days to 3.5 days. Following the previous observation [Del Genio and Rossow, 1990], we can consider this periodical phenomena as the propagation of planetary-waves. The phase velocity can be calculated about 85 m/s in OP1 and otherwise 125 m/s in OP5 and OP6. Latter velocity is faster than ever discovered. Recently, some studies show the mean zonal velocity derived from cloud tracking method become faster than ever [Khatuntsev et al., 2013; Kouyama et al., 2013]. These studies show that the mean zonal flow is accelerated more than 30 m/s from 2006 to 2012 and finally it reach about 120 m/s. This zonal flow is a little faster than the Pioneer Venus observed (Figure 1.9). In general, the mean zonal flow and planetary waves are non-linearly-coupled therefore it should be appropriate that our result suggests the 3.5 days fast periodicity. Figure 5.1 displays the results of fitting sin curve for the UV brightness variation (same data as analyzed in section 4.3). Periods, amplitudes and phases are estimated from the equations in Appendix D. We can find clear sinusoidal variations in the data from OP1. Figure 5.2 is the similar diagram but note that the fitted sin curve is drawn only by using OP5 data. The fitted sin curve not only coincide with the data from OP5 but also with the data from OP6. Therefore we suppose that the periodical variation in both OP5 and OP6 is the same wave. The spectrum power slightly decrease from OP5 to OP6, but our result suggests the 3.5 days wave last at least for two months. As our conclusion, the periodical brightness variation, which caused by planetary wave, last for over 2 months. However this periodic nature could be change with the time scale less than 1 Venus year (timing difference between August 2013 and May 2014 is about 9 months). When we assume the single acceleration phase exist within the time between OP1 and OP5, our observations give a hint that the lower limit of that time scale is 9 months. At the same time, we can assume one and a half cycle of acceleration and deceleration phase exist. In this case, the lower limit of the time scale of periodicity change is 3 months.

Next we discuss about the emergence of HY-feature. In OP2 and OP3, there are HY-features which is the Y-feature pattern such as the analyzed Galileo data show, last only for 1-1.5 phase. Lomb-Scargle analysis results suggest that the power spectrum is not single peaked but double peaked (Figure 4.11, 4.12) which over 90 % significant level in the period range from 3 to 7 days. The result from OP1 rather has double peaks and the contour results (Figure 4.4) also seems to have HY-feature. From these facts, we

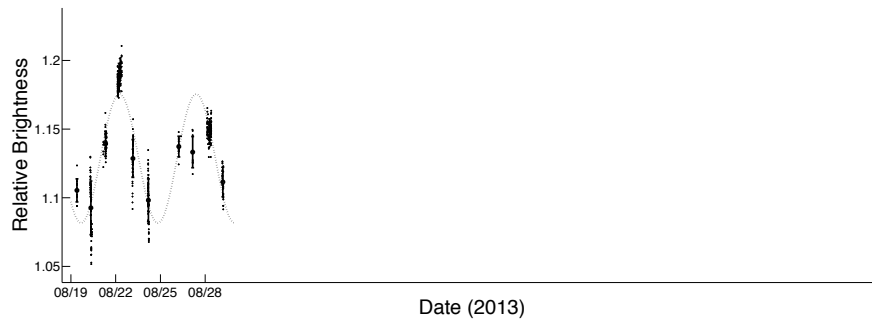


Figure 5.1: About 5.2 days periodical change appears in the data of OP1. The plotted sine curve (dashed line) is derived from Lomb-Scargle analysis.

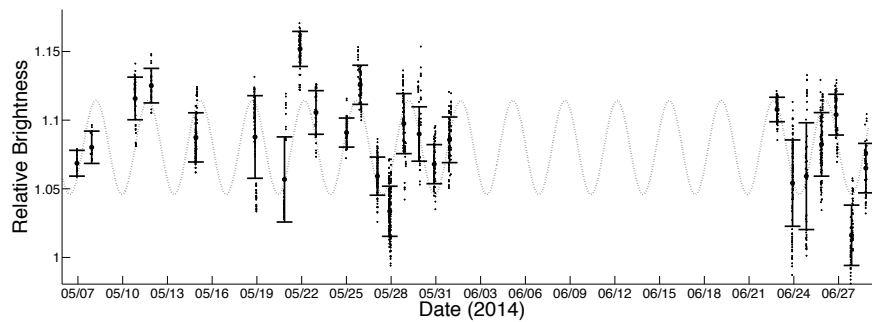


Figure 5.2: About 3.5 days periodical change appears in the data of OP5 and OP6. The plotted sine curve (dashed line) is derived only with the data from OP5 and just extended up to the last day in OP6.

consider that the HY-feature is caused by two wave modulation. Our consideration follow the simulation results by Yamamoto and Tanaka (1997b) (Figure 1.14). They argue that about 4 and 5 days planetary waves modulate and cause a few weeks fluctuation. Our normalize analysis technique (described in Section 3.5) might affect brightness variation in equatorial region (from  $10^{\circ}\text{N}$  -  $10^{\circ}\text{S}$ ) by the periodical variation in mid-latitudinal area. Therefore, results of double peaked periodgram and spectrum peak is in  $\sim 10$  days can be caused by a few weeks modulated Y-feature. Since our observed fact is that the 5.2 days periodicity had changed to 3.5 days periodicity after sending the season when the two waves coupled and make HY-feature. It might be regarded that the modulation of two planetary waves accelerate the Venus atmosphere.

## 6 Summary

We investigate the variability of the Venus UV brightness from long-term ground-based observation using Pirka telescope. We have six observational period and each one is continuous observation for one month. Our ground based results with the original reduction technique can reconstruct the similar brightness variation with VMC's in southern hemisphere. We have two observational periods when the brightness has the prominent periodical variation. Latter season is considered to keep the periodicity for about two months. In August 2013, we detected about 5.2 days periodical brightness variation in equatorial and both northern and southern mid-latitudinal region. Bright and dark pattern had a prominent periodical and symmetric structure about the equator and we consider it is derived from a Y-feature such as previously observed by the Galileo spacecraft. On the other hand, after the mid-September 2013, there was no prominent and periodical brightness variation in the most of the observation time. In this season, the periodical and symmetric brightness structure has a cycle of being clear and unclear, and it suggests the Y-feature has a few weeks variation (HY-feature). From mid-September 2013 to the end of March 2014, periodical variation seems to be lost or one more accelerate and decelerate cycle should exist. In the last two months (from the beginning of May to the end of June 2014), however, it has 3.5 days period and perhaps last for about two months. Our study points out the possibility of the change of dynamical states occur in one Venus year. Del Genio and Rossow, (1990) reported the dynamical state change with the time scale about 5-10 years, however our results suggest shorter time scale typically 3-9 months. And also we observe the acceleration of phase velocity after sending the season when the HY-feature exist. Since the HY-feature can be considered as the two planetary wave modulation, our study support the theory that the planetary waves have great contribution to forming Venus super-rotation as previously simulated by Yamamoto and Tanaka, (1997a).

## Acknowledgment

The author deeply grateful for the instruction for the scientific study by Prof. Yukihiro Takahashi.

I also appreciate to Dr. Makoto Watanabe for his assists for my observation and to Dr. Toru Kouyama for helpful discussions.

I have had the support and encouragement from all member of the PSG group of Hokkaido Univ.

And finally, I would like to express my gratitude to the staff of Nayoro observatory for their support my stay in the observation.

## Appendix

### A: Measurement error of brightness variation

Discrepancies of the determined geographical coordinates cause some differences of the calculated brightness values from original ones. These differences are checked in a quantitative way against one standard deviation of original data. Tests were conducted for  $\pm 1$  pixel discrepancies for each X and Y directions as the function of latitude. From this check process, we can find the discrepancies for the Y direction double the deviation of data value. However as already described in Section 3.3, images with discrepancies larger than 1 pixel are expected less than 5%. Therefore, we conclude that the determination discrepancies are not critical for our study.

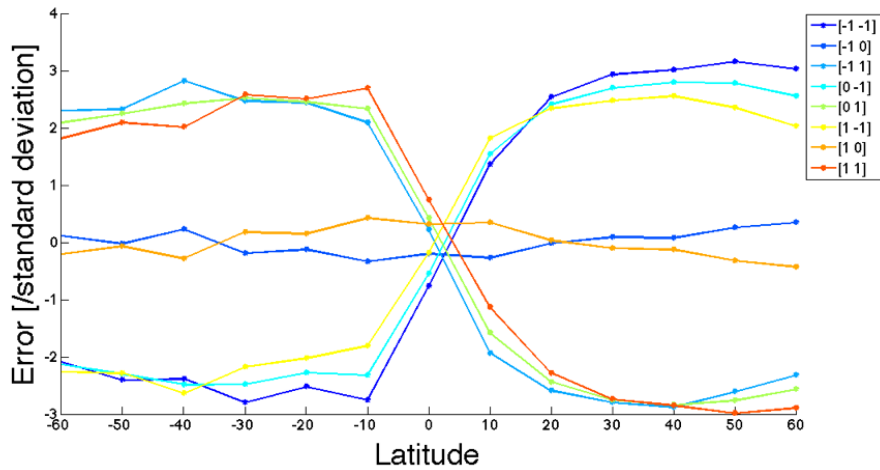


Figure .1: Measurement error in data observed in August 22, 2013 caused by the discrepancies of the determined geographical coordinates (normalized with one standard deviation of original data) as the function of latitudes.

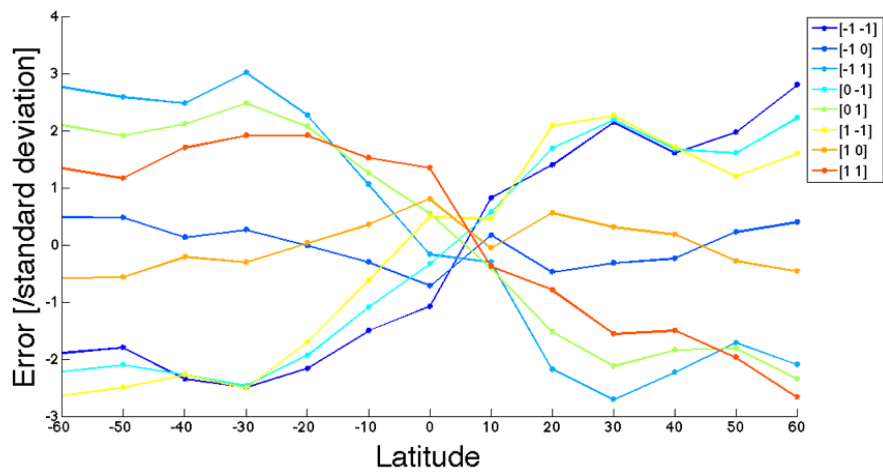


Figure .2: Measurement error in data observed in October 6, 2013 caused by the discrepancies of the determined geographical coordinates (normalized with one standard deviation of original data) as the function of latitudes.

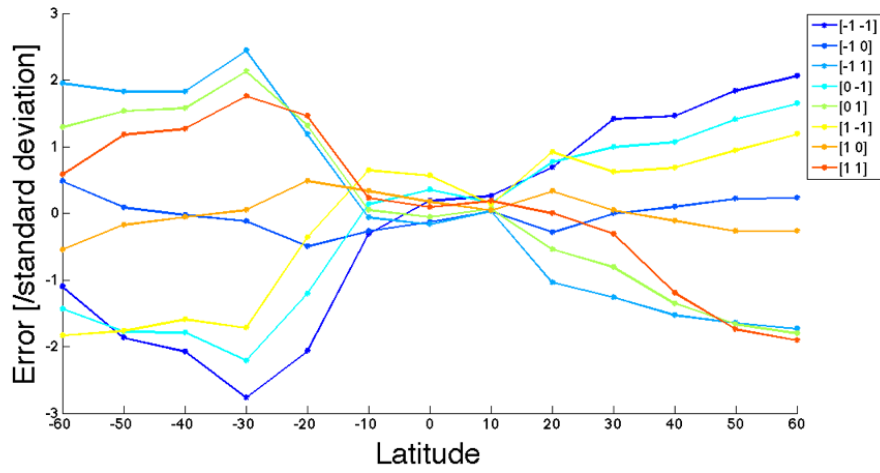


Figure .3: Measurement error in data observed in November 1, 2013 caused by the discrepancies of the determined geographical coordinates (normalized with one standard deviation of original data) as the function of latitudes.

**B: List of analyzed Galileo/SSI images**

Image NO.	Date	Time (UT)
18494400	1990-02-13	05:58:17
18633900	1990-02-14	05:28:47
18773300	1990-02-15	04:58:16
18912800	1990-02-16	04:28:46
19052200	1990-02-17	03:58:15

## C: List of analyzed Venus Express/VMC images

Image NO.	Date	Time (UT)	SSLON	SSLAT	SSCLON	SSCLA
V2676_0044_UV2	2013-08-18	02:43:45	68.47	-0.01	117.04	-79.76
V2677_0004_UV2	2013-08-18	23:20:10	71.11	0.05	-57.18	-88.14
V2678_0040_UV2	2013-08-20	02:36:34	74.61	0.13	120.01	-80.55
V2679_0012_UV2	2013-08-21	01:58:29	77.60	0.20	121.20	-83.34
V2680_0025_UV2	2013-08-22	02:49:24	80.78	0.28	123.11	-79.81
V2681_0004_UV2	2013-08-22	23:25:49	83.42	0.34	-51.84	-88.10
V2682_0025_UV2	2013-08-24	02:52:13	86.93	0.42	126.13	-79.83
V2683_0012_UV2	2013-08-25	02:04:08	89.90	0.49	127.31	-83.39
V2684_0025_UV2	2013-08-26	02:55:02	93.09	0.57	129.17	-79.86
V2685_0012_UV2	2013-08-27	02:06:57	96.05	0.64	130.37	-83.42
V2686_0025_UV2	2013-08-28	02:57:53	99.23	0.71	132.20	-79.89
V2687_0025_UV2	2013-08-29	03:00:48	102.31	0.78	133.72	-79.79
V2688_0025_UV2	2013-08-30	02:55:43	105.37	0.85	135.20	-80.31
V2689_0025_UV2	2013-08-31	02:57:08	108.44	0.92	136.71	-80.32
V2711_0052_UV2	2013-09-22	04:13:56	176.06	2.17	169.70	-79.19
V2712_0092_UV2	2013-09-23	04:01:41	179.10	2.21	171.14	-80.14
V2713_0092_UV2	2013-09-24	04:02:08	-177.83	2.25	172.60	-80.09
V2714_0092_UV2	2013-09-25	04:03:18	-174.76	2.28	174.07	-80.05
V2715_0092_UV2	2013-09-26	04:04:51	-171.70	2.32	175.53	-80.06
V2716_0080_UV2	2013-09-27	04:11:26	-168.62	2.35	177.01	-79.68
V2717_0048_UV2	2013-09-28	04:18:01	-165.54	2.38	178.49	-79.29
V2718_0044_UV2	2013-09-29	04:10:36	-162.49	2.41	179.92	-80.03
V2719_0044_UV2	2013-09-30	04:06:10	-159.44	2.44	-178.64	-80.52
V2720_0048_UV2	2013-10-01	04:22:45	-156.34	2.47	-177.13	-79.35
V2721_0048_UV2	2013-10-02	04:24:20	-153.27	2.49	-175.68	-79.37
V2722_0048_UV2	2013-10-03	04:25:55	-150.21	2.52	-174.22	-79.38
V2723_0028_UV2	2013-10-04	04:27:30	-147.14	2.54	-172.77	-79.40
V2724_0028_UV2	2013-10-05	04:29:04	-144.07	2.55	-171.32	-79.42
V2725_0048_UV2	2013-10-06	04:30:39	-141.01	2.57	-169.87	-79.43
V2726_0024_UV2	2013-10-07	03:37:15	-138.06	2.59	-168.76	-83.49
V2728_0040_UV2	2013-10-09	03:35:26	-131.93	2.61	-165.95	-83.85
V2730_0040_UV2	2013-10-11	03:38:38	-125.80	2.62	-163.10	-83.87
V2736_0028_UV2	2013-10-17	04:32:17	-107.30	2.62	-154.09	-80.84
V2737_0040_UV2	2013-10-18	04:49:54	-104.20	2.62	-152.52	-79.60
V2738_0028_UV2	2013-10-19	04:35:30	-101.16	2.61	-151.20	-80.87
V2739_0018_UV2	2013-10-20	04:43:07	-98.08	2.60	-149.71	-80.42
V2740_0032_UV2	2013-10-21	04:58:43	-94.98	2.58	-148.15	-79.31
V2742_0018_UV2	2013-10-23	04:47:54	-88.87	2.55	-145.38	-80.45
V2743_0022_UV2	2013-10-24	04:39:29	-85.82	2.53	-144.03	-81.23
V2744_0004_UV2	2013-10-25	00:51:03	-83.24	2.51	40.62	-85.90
V2745_0018_UV2	2013-10-26	04:52:37	-79.66	2.49	-141.04	-80.48
V2746_0018_UV2	2013-10-27	04:54:11	-76.59	2.46	-139.59	-80.49
V2747_0018_UV2	2013-10-28	04:55:45	-73.52	2.43	-138.14	-80.50
V2748_0018_UV2	2013-10-29	04:42:18	-70.48	2.41	-136.86	-81.65
V2749_0018_UV2	2013-10-30	04:43:51	-67.41	2.37	-135.41	-81.66
V2750_0018_UV2	2013-10-31	04:45:23	-64.33	2.34	-133.96	-81.66
V2751_0018_UV2	2013-11-01	04:46:55	-61.26	2.31	-132.51	-81.67
V2752_0018_UV2	2013-11-02	04:48:26	-58.19	2.27	-131.06	-81.68
V2753_0018_UV2	2013-11-03	04:49:57	-55.12	2.23	-129.61	-81.69
V2754_0018_UV2	2013-11-04	04:51:27	-52.04	2.19	-128.15	-81.70
V2755_0018_UV2	2013-11-05	04:52:58	-48.97	2.15	-126.70	-81.71
V2756_0018_UV2	2013-11-06	04:54:29	-45.90	2.11	-125.24	-81.71
V2757_0018_UV2	2013-11-07	04:55:59	-42.82	2.07	-123.78	-81.72
V2758_0018_UV2	2013-11-08	04:52:29	-39.76	2.02	-122.40	-82.09
V2759_0018_UV2	2013-11-09	05:14:59	-36.64	1.97	-120.65	-80.53

## D: Lomb-Scargle periodgram analysis

Lomb-Scargle method calculates the spectral power (P) at an angular frequency  $\omega$  from evenly or non-evenly spaced data points  $X_j = X(t_j), j = 1, \dots, N$  as (Scargle, 1982). Here X are subtracted values by its arithmetic average ( $1/N \cdot \sum X$ ).

$$P(\omega) = \frac{1}{2} \left\{ \frac{\left[ \sum_j X_j \cos \omega(t_j - \tau) \right]^2}{\sum_j \cos^2 \omega(t_j - \tau)} + \frac{\left[ \sum_j X_j \sin \omega(t_j - \tau) \right]^2}{\sum_j \sin^2 \omega(t_j - \tau)} \right\} \quad (15)$$

where  $t_j$  is time. Here  $\tau$  is defined by the relation

$$\tan(2\omega\tau) = \frac{\sum_j \sin 2\omega t_j}{\sum_j \cos 2\omega t_j}. \quad (16)$$

This procedure is equivalent to a linear least-squares fitting of the function

$$X(t) = a \cos\{\omega(t - \tau)\} + b \sin\{\omega(t - \tau)\} \quad (17)$$

to the analyzed data (Scargle, 1982), where a and b are obtained by equations below respectively.

$$a = \frac{\sum_j X_j \cos \omega(t_j - \tau)}{\left\{ \sum_j \cos^2 \omega(t_j - \tau) \right\}^{1/2}} \quad (18)$$

$$b = \frac{\sum_j X_j \sin \omega(t_j - \tau)}{\left\{ \sum_j \sin^2 \omega(t_j - \tau) \right\}^{1/2}} \quad (19)$$

Then, the amplitude A is obtained by the following equation.

$$A = \sqrt{a^2 + b^2}, \quad (20)$$

and the phase at  $t = 0$  is calculated by

$$X(t) = A \sin \left\{ \omega(t - \tau) + \tan^{-1} \left( \frac{a}{b} \right) \right\}. \quad (21)$$

---

## References

- [1] Belton, M. J. S., P. J. Gierash, M. D. Smith, P. Helfenstein, P. J. Schinder, J. B. Pollack, K. A. Rages, D. Morrison, K. P. Klaasen, and C. B. Pilcher (1991), Images from Galileo of the Venus cloud deck, *Science*, 253, 1531-1536.
- [2] Bertaux, J., T. Widemann, A. Hauchecorne, V. I. Moroz, and A. P. Ekonomov (1996), VEGA 1 and VEGA 2 entry probes: An investigation of local UV absorption (220-400 nm) in the atmosphere of Venus (SO<sub>2</sub>, aerosols, cloud structure), *J. Geophys. Res.*, 101, 12709-12745.
- [3] Del Genio, A. D., and W. B. Rossow (1982), Temporal variability of ultra-violet cloud features in the Venus stratosphere, *Icarus*, 51, 391-415.
- [4] Del Genio, A. D., and W. B. Rossow (1990), Planetary-scale waves and the cyclic nature of cloud top dynamics on Venus, *J. Atmos. Sci.*, 47, 293-318.
- [5] Dollfus, A. (1975), Venus: Evolution of the Upper Atmospheric Clouds, *J. Atmos. Sci.*, 32, 1060-1070.
- [6] Esposito, L. W. (1980), Ultraviolet contrasts and the absorbers near the Venus cloud tops, *J. Geophys. Res.*, 85(A13), 8151-8157.
- [7] Khatuntsev, I.V., Patsaeva, M.V., Titov, D.V., Ignatiev, N.I., Turin, A.V., Limaye, S.S., Markiewicz, W.J., Almeida, M., Roatsch, Th., Moissl, R., 2013. Cloud level winds from the Venus Express Monitoring Camera imaging. *Icarus* 226, 140-158.
- [8] Kliore, A. J. and I. R. Patel, Vertical structure of the atmosphere of Venus from Pioneer Venus orbiter radio occultations, *J. Geophys. Res.*, 85, 7957-7962, 1980.
- [9] Kouyama, T., T. Imamura, M. Nakamura, T. Satoh, and Y. Futaana (2012), Horizontal structure of planetary-scale waves at the cloud top of Venus deduced from Galileo SSI images with an improved cloud-tracking technique, *Planet Space Sci.*, 60, 207-216.
- [10] Kouyama, T., Imamura, T., Nakamura, M., Satoh, T., Futaana, Y. (2013), Long-term variation in the cloud-tracked zonal velocities at the cloud top of Venus deduced from Venus Express VMC images, *J. Geophys. Res.*, 118, 37-46.

- 
- [11] Lomb, L. R. (1976), Least-squares frequency analysis of unequally spaced data, *Ap. Scace Sci*, 39, 447-462.
- [12] Machado, P., D. Luz, T. Widemann, E. Lellouch, and O. Witasse (2012), Mapping zonal winds at Venus's cloud tops from ground-based Doppler velocimetry, *Icarus*, 221, 248-261.
- [13] Molaverdikhani, Karan; McGouldrick, Kevin; Esposito, Larry W. (2012), The abundance and vertical distribution of the unknown ultraviolet absorber in the venusian atmosphere from , sis of Venus Monitoring Camera images, Issue 217,648-660.
- [14] Ogohara, K., T. Kouyama, H. Yamamoto, N. Sato, M. Takagi, and T. Imamura (2012), Automated cloud tracking system for the Akatsuski Venus Climate Orbiter data, *Icarus*, 217, 661-668.
- [15] Peralta, J., R. Hueso, and A. Sanchez-Lavega (2007a), Cloud brightness distribution and turbulence in Venus clouds using Galileo violet images, *Icarus*, 188, 305-314.
- [16] Peralta, J., R. Huseo, and A. Sanchez-Lavega (2007b), A reanalysis of Venus winds at two cloud levels from Galileo SSI images, *Icarus*, 190, 469-477.
- [17] Rossow, W. B., A. D. Del Genio, S. S. Limaye, L. D. Travis, and P. H. Stone (1980), Cloud morphology and motions from Pioneer Venus images, *J. Geophys. Res*, 85, 8107-8128.
- [18] Rossow, W.B., A. D. Del Genio, T. P. Eichler (1989), Cloud-tracked winds from pioneer Venus OCPP images, *J. Atmos. Sci.*, 47, 2053-2084.
- [19] Scargle J. D. (1982), Studies in astronomical time series analysis. II - Statistical aspects of spectral analysis of unevenly spaced data, *Astrophys. J.*, 263, 835-853.
- [20] Schubert, G., et al. (1980), Structure and circulation of the Venus atmosphere, *J. Geophys. Res.*, 85, 8007-8025.
- [21] Titov, D. V., et al. (2012), Morphology of the cloud tops as observed by the Venus Express Monitoring Camera, *Icarus*, 217, 682-701.
- [22] Travis, L. D., D. L. Coffeen, J. E. Hansen, K. Kawabata, A. A. Lacis, W. A. Lane, S. S. Limaye, and P. H. Stone (1979), Orbiter cloud photopolarimeter investigation, *Science*, 203, 781-785.

- [23] Watanabe, M., Y. Takahashi, M. Sato, S. Watanabe, T. Fukuhara, K. Hamamoto, A. Ozaki (2012), MSI: visible multi-spectral imager for 1.6-m telescope of Hokkaido University, SPIE, 8446, 84462O-84462O-10.
- [24] Yamamoto, M., and H. Tanaka (1997a), Formation and maintenance of the 4-day circulation in the Venus middle atmosphere, *J. Atmos. Sci.*, 54, 1472-1489.
- [25] Yamamoto, M., and H. Tanaka (1997b), The Venusian Y-shaped cloud pattern based on an aerosol-transport model. *J. Atmos. Sci.*, 55, 1400-1416.